PURDUE UNIVERSITY
GRADUATE SCHOOL
Thesis/Dissertation Acceptance

This is to certify that the thesis/dissertation prepared

By Ameya Kulkarni

Entitled
AU NANOPARTICLE ASSEMBLY ON CNTS USING FLASH INDUCED SOLID-STATE DEWETTING

For the degree of   Master of Science in Mechanical Engineering

Is approved by the final examining committee:

Jong Eun Ryu
Chair

Mangilal Agarwal

Jian Xie

Ruihua Cheng

To the best of my knowledge and as understood by the student in the Thesis/Dissertation Agreement, Publication Delay, and Certification Disclaimer (Graduate School Form 32), this thesis/dissertation adheres to the provisions of Purdue University's "Policy of Integrity in Research" and the use of copyright material.

Approved by Major Professor(s): Jong Eun Ryu

Approved by: Sohel Anwar   4/28/2015

Head of the Departmental Graduate Program   Date

AU NANOPARTICLE ASSEMBLY ON CNTS USING FLASH INDUCED

SOLID-STATE DEWETTING

A Thesis

Submitted to the Faculty

of

Purdue University

by

Ameya Kulkarni

In Partial Fulfillment of the

Requirements for the Degree

of

Master of Science in Mechanical Engineering

May 2015

Purdue University

Indianapolis, Indiana

ACKNOWLEDGMENTS

I would like to express my gratitude to my committee chair Prof. Jong Ryu, without his guidance and persistent help this research and thesis would not have been possible.

Besides my advisor, I also wish to thank my committee members Prof. Mangilal Agarwal, Prof. Ruihua Cheng and Prof. Jian Xie for serving in the evaluating committee.

I am thankful to members of Integrated Nanosystems Development Institute, Dr. Daniel Minner and Dr. Sudhir Shreshtha for their advice and cooperation during my research tenure. Also I thank Dr. Sohel Anwar and the entire staff of the Department of Mechanical engineering for their assistance.

Finally, I would like to thank my family for their love and unconditional support during the last two years.

TABLE OF CONTENTS

iv

Page

LIST OF TABLES

LIST OF FIGURES

ABSTRACT

Kulkarni, Ameya. M.S.M.E., Purdue University, May 2015. Au Nanoparticle Assembly On CNTs Using Flash Induced Solid-State Dewetting. Major Professor: Jong Eun Ryu.

Carbon Nanotubes (CNTs) are used extensively in various applications where substrate are required to be possessing higher surface area, porosity and electrical and thermal conductivity. Such properties can be enhanced to target a particular gas and biochemical for efficient detection when CNT matrix is functionalized with Nanoparticles (NPs). Conventional functionalization involves harsh oxidation repeated washing, filtration and sonication, which induce defects. The defects lead to hindered mobility of carriers, unwanted doping and also fragmentation of the CNTs in some cases. In this document we demonstrate functionalization of CNT with Au nanoparticles on a macro scale under dry and ambient condition using Xenon flash induced solid-state dewetting. A sputtered thin film was transformed into nanoparticles which were confirmed to be in a state of thermodynamic equilibrium. We worked on 3 nm, 6 nm, 9 nm, 15 nm, 30 nm initial thickness of thin films. Xenon flash parameters of energy, number of pulse, duration of pulse, duration of gap between consecutive pulses were optimized to achieve complete dewetting of Au thin films. 3 nm deposition was in the form of irregular nano-islands which were transformed into stable nanoparticles with a single shot of 10 J/cm^2 of 2 ms duration. 6 nm and 9 nm deposition was in form of continues film which was also dewetted into stable nanoparticles with a single pulse but with an increased energy density of 20 J/cm^2 and 35 J/cm^2 respectively. In case of 15 nm and 30 nm deposition the thin film couldnt be dewetted with a maximum energy density of 50 J/cm^2, it was observed that 3 and 4 pulses of 2 ms pulse duration and 2 ms gap duration with an energy density of 50 J/cm^2 were required to completely dewet the thicker films. However

irregularity was induced in the sizes of the NPs due to Ostwald ripening phenomenon which causes smaller particle within a critical diffusion length to combine and form a larger particle during or after dewetting process. For comparison, the Au thin films were also dewetted by a conventional process involving annealing of samples until the thin film was fully transformed into NPs and the size of NPs seized to grow. Scanning electron microscope (SEM) was used to characterize the samples. Thermodynamic stability of the particles was confirmed with statistical analyses of size distribution after every additional pulse.

1. INTRODUCTION

1.1   Nanoparticle Based Systems

Employing nanoparticles offer tangible opportunities to improve the current technologies and explore new possibilities. Since the last half a century, efforts are put in to develop newer and newer applications. We have reached a stage where we use nanoparticles in our day to day lives. Some of these products are the sunscreen lotion, which uses titanium and zinc oxide nanoparticles [1], another example of a very common application is of the batteries [2]. Batteries use vanadium oxide nanoparticles as anode material to improve cyclic performance [3]. Energy based application are the prime users of nanoparticles, the application also include solar cell and capacitors [4,5]. Another major industry which makes use of nanoparticles is of the medical technologies, from drug delivery and cancer diagnosis to glucometers nanoparticles are widely used [6–8]. To offer an insight into what nanoparticles are, the next section presents a brief explanation.

1.2   Nanoparticles

Nanoparticles can be considered as building blocks of many nanotechnological applications. Nanoparticle are accumulation of particles ranging from 1 nm to 1000 nm. At the nanoscales the properties of the material vary significantly as compared to their bulk counterparts. This is mainly due to higher surface to volume ratio and quantum confinement [9]. Due to these, properties of thermodynamic stability and balanced surface energy, nanoparticles are extensively used in energy based application such as batteries, capacitors and fuel cells [2,10,11]. The larger surface area and optical properties make them very useful in solar cell based application [4]. Also the electronics and photonic properties have led them use in technologies such as plasmon resonance

and quantum dots for diagnostic and characterization application [8, 12]. Nanoparticles have excellent electrical properties, the use of nanoparticles enhances mobility of carriers increasing electronic efficiency of the systems [13]. In batteries, nanoparticle are anchored on the anode material that result in higher columbic efficiency, better rate capability, excellent cyclic performance, large reversible capacity [2]. Silver nanoparticles are reported to be used in capacitors, owing to their capabilities of decreasing dissipation losses and increasing dielectric constant [10]. Nanoparticles are used on sensors and drug delivery systems, due to their chemical properties such as selectivity and ultra-high sensitivity [6, 12]. Nanoparticles enable effective detection and identification of gases by using low power sensors.

More often than not, nanoparticles have to be supported on a structure acting as base. Such a support structure can be in form of a liquid solution or solid substrate. One of the important support structures or substrate material is CNTs. The next section tries to explain what CNTs are and why are they so significant.

1.3 CNTs

Owing to the different hybridization capabilities, carbon can be exist in various allotropic forms. Allotropic forms of carbon can be 0, 1, 2 and three dimensional. Out of these the two dimensional form of carbon allotrope is called the carbon nanotube (CNT). CNTs can be imagined as a roll of graphene sheet. CNTs are categorized into two types:

1. Single Walled CNTs (SWCNTs)

2. Multi Walled CNTs (MWCNTs)

CNTs are made of two structures, the cylindrical structure is called the side wall which is usually made of benzene like structures. And the caps at the ends are two semi-spherical fullerene like molecules.

SWCNTs are structured to have a single wall made from rolling a single graphene sheet. Their diameter ranges between 0.7 to 1.4 nm depending on their synthesis

temperature. MWCNTs are composed of multiple graphene layer stacked onto one another, a rolled up structure of such a sheet makes a multi-walled carbon nanotube. MWCNTs can have diameter up to 100 nm.

CNTs are intensively researched on due to their attributes such as high surface area, extremely high mechanical strength, ultra-light weight, high thermal conductivity, electrical stability and chemical selectivity [14, 15].

To make use of such a substrate and to enhance its properties for the above mentioned application, nanoparticles have to be support on carbon nanotube. This process of adding nanoparticles to substrates is called functionalization of substrates. In this research carbon nanotube are used as substrates and the next section discusses some of the important methods used today for functionalization of CNTs.

1.4 Functionalization Methods

Functionalization of CNTs can be classifies using various schemes. One of the schemes which is more of an industry oriented or is physical classification of methods of functionalization. The schemes classifies the methods into wet and dry methods of functionalization. This scheme discusses the various methods used for both dry physical vapor deposition and wet chemical depositions treatments which are most popular. The methods discussed are applied to various substrates and not only CNTs.

1.4.1 Physical Vapor Deposition Methods

The physical vapor deposition methods, often referred to as dry methods. Some of the most popular methods in this category are:

Laser Induced Dewetting

In this technique *Favazza* used the energy source as a laser and accounted the evolution of nanoparticles [16]. In the experiments which were performed an initial

film thickness of 1 to 8 nm was used the rates being 0.5 to 2 nm per second. The substrate used in this case was Si/SiO_2 wafers. Silicon oxide was thermally grown on the substrates. A laser of 266 nm wavelength was used to dewet the thin film. Metal concentration on the substrate was measured by dispersive X-ray spectroscopy in a scanning electron microscope. This value of concentration was calibrated to corresponding film thickness by the step height and Rutherford backscattering measurements of the thin film. The film surface was treated with laser in a vacuum immediately after deposition with an unfocussed 3 x 3 mm^2 laser beam. In such a process the temperature of approximately 500K was estimated to have been exceeded from the normal melting point of the metal. To account for the evaporation of metal and the mass loss, good approximation of $\leq 15\%$ was accounted considering the highest amount of laser induced energy and the laser time interval.

Thermal Annealing

Tesler demonstrated this method in which they studied the dewetting process of just percolated Au films [17]. They used substrate as glass and studied the morphological evolution of nanoparticles. In such a method of synthesis induced energy was thermal and Au thin films of initial thickness of 10 nm to 16 nm was used. Borosilicate glass slides of 9 cm x 22 cm were used. The slides were cleaned with piranha solution of remove all organic impurities, after which they were sonicated to get rid of any non-organic residue. Once the residue was removed the glass slides were rinsed with distilled water and dried in nitrogen stream. A resistive evaporation technique was used to deposit Au at the rate of 0.005 nm to 0.01 nm per second. To get a uniform thickness the glass slide were chucked to a rotating holder and a homogeneous thin film was obtained. The film thickness was varied from 10 nm to 16 nm. Once the slides were coated a regular annealing process was done to using an oven for different periods of time. Glass slides were annealed from a time range of 20 minutes to 10 h. The oven was preheated to 550 °C. An approximate drop of 150 °Cwas observed dur-

ing the loading and unloading of the samples which was recovered within 300 seconds. The last batch of 10 h of annealing time were cooled in the oven itself by atmospheric convection. UV-vis spirometer was used to generate spectra of the Au films. HRSEM was used to image the samples at working distance of 3 mm with 2 kV voltage. TEM was also used to image the samples. AFM and XRD measurements were carried out as to estimate the average radius and the crystalline size of the films.

Focused ion beam deposition

This technique is reported by Zhou wherein they have used focused ion beam to induce energy on the Au thin film [5]. The Au thin film is sputter on the carbon film which is used as a substrate for this experiments. The imaging is done using SEM, AFM and TEM. Au films were coated on the substrate in a sputter with 10mbar pressure. The ion bombardment was carried out with dual beam FIB Ga^+ ions in a vacuum of $2x10^{-7}$ mbar at room temperature. The electron beam attached this FIB has a resolution of 1.5 nm which was also used for in situ imaging for SEM. The Au film was obtained by sputtering at a current of 8mA for 60s and had a thickness of 8 nm which was estimated using AFM step analysis. AFM was also used to confirm the uniformity of the Au nanoparticles. Such a method could obtain a uniformly distributed 10 nm nanoparticles.

Sacrificial Layer Assisted Dewetting

In such a process sample is prepared by deposition of a sacrificial layer first and then the actual Au film is deposited. Such a process if often termed as a supported Au nanoparticle dewetting [18]. After the deposition of sacrificial layer, in this case antimony the Au film is deposited. Such a deposition and support of antimony layer cause a change in dewetting characteristics which are influenced due to the simultaneous sublimation of the sacrificial layer. Once all the antimony is evaporated the Au nanoparticles are left in an immobilized state on the substrate. The experiments

for this technique were carried out using sapphire as a substrate, sapphire being an ideal choice considering its low surface energy, high thermal and chemical stability and crystallographic perfections. Also sapphire's high resistance to Au makes it an ideal substrate for inter diffusion. A film thickness on 0.7 nm to 24 nm was used to study the dewetting characteristics.

1.4.2 Wet Chemical Deposition Methods

Wet chemical deposition methods are as the name suggests, involve liquid reagents. These chemical are used for oxidative treatments which bond nanoparticles chemically together to the substrate. Following articles describe some of the popular methods which belong to this category.

Electrochemical Functionalization

Electrochemical functionalization is a process occurs at the electrode surface. The thickness and morphology of the coating layer can be controlled by factors such as deposition time, applied potential and concentration of the metal ions, electrolyte. Also parameters of solution such as pH, temperature, current density, agitation, applied potential needs to be monitored. Such a methods does not require a complex equipment set up and can be done near room temperature. Zhang and Nix demonstrated such a technique where they deposited PANI on SWCNTs for detection of ammonia and nitrogen di-oxide gas [19].

Thermal Activated Chemical Functionalization

Thermal activated chemical functionalization is another wet chemical process, it typically aims at producing carboxly groups which further assist in modification and act as nucleation sites. Such carboxly groups are introduced by oxidation treatments, amide and ester linkages can also be introduced on the side walls. Nucleophilic

reagents such as alcohols, amines, grignard reagents and alkyl lithium compounds are employed to produce functional groups on the side walls [20].

Microwave Assisted Chemical Functionalization

Microwave assisted chemical functionalization is a wet method involving a single step functionalization of multiwalled CNTs. Such methods aims at avoiding the use of harsh oxidative chemicals or sonication. This is an in situ method, and the nanoparticles are synthesized during functionalization by metal ion reduction. Raghuveer and Agarwal demonstrated such a process, where they functionalized CNTs in a single step process [21]. The combined used use of microwave radiation and polyol reduction of metal salt led to derivatize CNTs with Au nanoparticles. Microwave is used with an aim to create defect sites for formation of a functional groups in side walls of CNTs. The defect sites prove to be preferred nucleation sites reduction reaction activated using microwave irradiation.

Substrate Enhanced Electroless Functionalization

Substrate enhanced electroless deposition (SEED) is a method which involve transformation of metal substrates on which carbon nanotube is attached into nanoparticle. Qu and Dai demonstrated such a method where they could induce metal ions reduction whose redox potential is lower than that of the carbon nanotube [22]. A large variety of metal nanoparticles can be deposited on CNTs without use of an additional reducing agent. This process can be used for depositing nanoparticles on inner walls of CNTs. However such methods involves use of wet chemical agents typically an aqueous solution like chloroauric acid.

1.5   Technical Barriers

The above mentioned methods are currently used functionalization methods. Although they are used extensilvely, there are many disadvantages which need to be addressed one of the major disadvantages of these methods are that they are extremely time consuming. A dewetting process by thermal annealing can take hours of process time, also the post annealing cooling time has to be taken into account. Such a process is inefficient for mass production or roll to roll production. Another major advantages with the process like ion beam or redisposition is that the sample size is a constraint, although time involved is not a major factor of concern [23]. A similar issue exist with the laser annealing process, as the tiny laser beam has to follow a rasterization technique to cover a large area, in turn increasing the process time [24]. All these methods cannot be realized for mass manufacturing or roll to roll production.

Wet chemical deposition methods, although scalable are accompanied with many disadvantages. These methods primarily involve harsh oxidative treatments to produce functional groups. Such treatments involve degradation of in mechanical properties of CNTs [25]. Also due to the induced defects, mobility of the carriers is significantly hindered. Creation of defect sites result in unwanted doping which is undesirable [26]. Often wet chemical deposition treatments involve long sonication treatments due to which CNT fibers are fragmented. Another common issue with chemical methods is that impurities generated by the process. Due to the use of chemical reagents, the output is never in a pure form and always possess some residue [27]. Agglomeration of particles is another issue. Due to the use of liquid reagents nanoparticles agglomerate into one larger particles loosing surface area and other morphological properties [28].

1.6 Motivation and Approach

Considering the above technical barriers, it was important we develop a method which eliminate the disadvantages and offer a convenient single step process. Such a process needed to be quick involving no long operation h and cooling or settling time unlike the thermal dewetting process. Also the method needed to be scalable in order to facilitate mass production or roll to roll production. Not only was mass production important, but it was also important to induce scalability. Scalability can be referred to as increasing the size of sample. All the above factors needed to be considered and a dry process was required to be designed.

Also for using substrates such as polymer and other organic material it was important that the temperature of the substrate remained low during the functionalization so as to prevent any damage due to heating. A dry process reduces defects and thus does not affect the mobility carrier, which is of utmost importance in the semiconductor industry. Also a dry process involves no drying or settling time and is free of residue. Another advantage of a dry process comes from the fact that often clean room is not required for such operation.

Thus such an approach was kept in mind to develop a quick, dry and scalable process.

2. BACKGROUND STUDY

2.1 History of Dewetting

The process of dewetting is studied since the last two decades. In the primitive studies, dewetting of liquids was major interest of study. Dr. W. Wick studied the dewetting of liquids with a microfluidic perspective [29].

The next logical step in the advancement of dewetting studies was, dewetting of one dimensional nano wires. Such research aimed at producing nanoparticles over a substrate. An array of metal was deposited by lithography and patterned into wires. These wire were then dewetted to form nanoparticles. Such a research was done by Fowlkes [30].

The next step consisted of creating sheets of nanoparticle decorated materials. For such a purpose a layer of material needed to be deposited and dewetted. Thus a two dimensional sheet of metal was then studied and Farzinpour demonstrated such a research [18].

2.2 Macroscopic Stages of Dewetting

The basic formation of the nanoparticles in a dry method is associated with two main processes. The first of these process is to create a thin layer of metal to be deposited on the substrate in this case gold. The thin film is created by physical vapor deposition or the sputtering process. Sputtering process creates a thin film and the material out of which the nanoparticle are to be formed is deposited in this way. The second process is that of inducing such kind of energy so as to initiate the dewetting process. The dewetting phenomenon is a process by which a thin film is transformed into nanoparticles. The formation is nanoparticles their density, size and population is a function of factors of wettability of the substrate surface,

which can be measured in contact angles by the goniometer, another important factor which contributes towards the dewetting process is the surface interaction between the deposited metal, that is gold and the substrate, which can be anything what the application demands. Generally experiments carried out on CNT, graphene and silicon are reported to be showing good results. Also the specific capacity of the gold has to be taken into account, so as to establish a relationship between the amounts of energy the film can absorb in a unit time period. Finally the method in which this energy is induced also varies the dewetting process. The thin film are in a metastable state and the dewetting process initiates with an irregularity or a hole in the film which leads to nucleation. Guntur studied the process [31], the micrographs of which are shown in Figure 2.1.
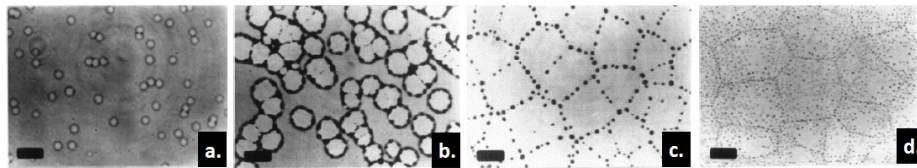
Figure 2.1. (a) Micrographs of the initial condition of thin film with irregularities, (b) Growth of holes on the substrate. (c) Formation of particles on the polygon edges and aligning in a particular shape (d) Uniform distribution of nanoparticles on further annealing [31].

Figure 2.1 (a) shows the initial film condition, the irregularly spaced white structures are the holes which randomly distributed. In section (b) holes have grown as the annealing process and material is collected at the hole boundary. Further annealing of energy induction leads formation of polygons of aligned nanoparticles which is shown in part (c) And in the final matured stage in a uniform distribution of nanoparticles across the substrate is observed. This study revealed as to how a thin film dewets on any substrate. Further the energy induced should also be accounted, as a minimum amount of energy is required to completely dewet the thin film. Also on inducing excess energy, it is observed that the particles evaporate and there is a mass loss from the substrate.
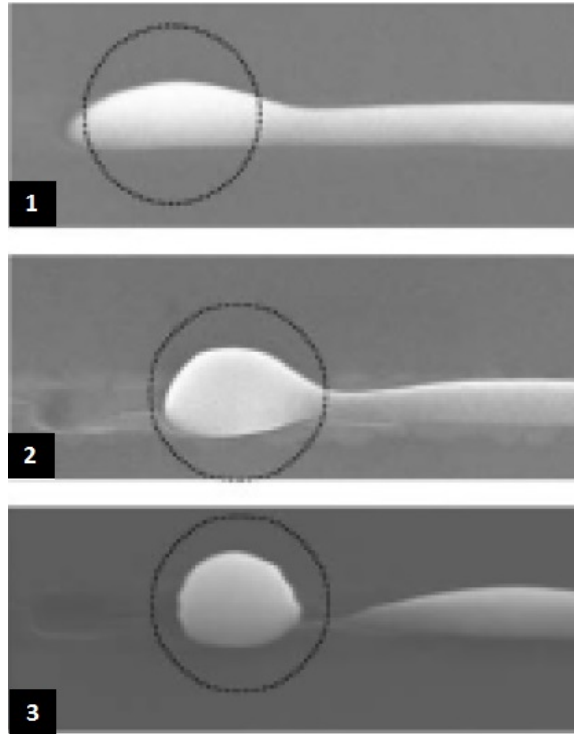
Figure 2.2. High resolution and tilted (45°) SEM images of the left edge of 55 nm thin metal lines after dewetting with laser after one, two and three pulses [32].

Figure 2.2 shows the SEM image of incompletely dewet particles. The figure is a single segment an array of nano structures. The first image is an incompletely dewet nano island, but as the induced energy increases, the thin film is completely dewet. This process is termed as pearling of particles. Beszada discussed the results of the effect of nanoparticles size when excess energy is induced, after the complete dewetting of particles [33].

They observe two effects on the particles if excess energy is input, after the complete dewetting of particles one of which is Ostwald ripening of particles. This phenomenon occurs when the energy is continued to input just after the complete dewetting of particles. In such a process the nanoparticles at certain distance apart fuse together to form larger nanoparticles. Also this process of fusing is often called ripening or the Ostwald ripening of the particles. This is first of the two process which

occur on excess energy input. The Ostwald ripening process continues to occur until all particles with the certain interparticle distance range are fused. It is to be noted that the interparticle distance is a function of the initial film thickness as well as the size of particles on complete dewetting.

Ostwald ripening is a phenomenon which can be characterized by Auger electron spectroscopy, the kinetics of which are can be realized and interpreted by models involving mass transport of ions and adatoms. The mass transport of adatoms is a function of surface diffusion coefficient D_{Si} and the surface diffusion length λ_{Si} [33]. The surface diffusion length can be obtained as a function of diffusion coefficient which is given by the following equation:

$$\lambda_S = (D_{Si} * \tau)^{1/2}$$

Also the following condition are prerequisite for the Ostwald ripening phenomenon to proceed. The condition are defined by Beke and Kaganovskii [34, 35] and are as below:

1. Surface diffusion fields of the islands are overlapping (average distance between the particles should be less than twice the diffusion length).

2. Evaporation of adatoms is responsible for decrease of the effective thickness (area covered by particles is less than the total area).

3. Detachment of the adatoms process is slower than the surface diffusion process.

On further inducing energy the particles evaporate and mass is lost. In this process the population and size of particles decreases. It should also be noted that the melting and evaporation temperatures at nanoscale are reduces and the in situ observations do not agree with the melting and evaporation temperatures of bulk gold.

2.3 Physics Behind Process of Dewetting

Danielson studied the process of dewetting and concluded two major factors for solid state dewetting [36]. He performed experiments with silicon deposited in silicon oxide samples He listed Cappilary edge instabillity and Rayleigh instbility [37], and discussed a model for agglomeration with five distinctive steps which are listed as below:

1. Critical void formation

2. Void edge thickning

3. Void edge breakdown

4. Void finger formation and growth

5. Island fomation.

The schmatics in Figure 2.3 portrays the steps listed above.

The first step in the process consists of the critical void formation. The radius of the void greater than that of the critical radius are called supercritical voids which cannot be restored by the film resulting in a hole formation. Another type of voids are those with radius lesser than the critical radius which are called subcritical voids and are restored by the film. Film edges and nucleated voids are part of unstable voids.

In the second step, due to the capillary edge instability, mass flows from edge to the flat region, which thickens the edge with time. There is piling of material along the moving void edge, increasing its thickness and making it further unstable.

Step 3 demonstrates the breakdown mechnism of the edge, owing to the Rayleigh instability. The thickned edge acts as a denser and less viscous liquid while the film acts as more viscous liquid trying to mix into each other. The mixture mechnism begins with formation of wavy paterns and proceeds into the next step.
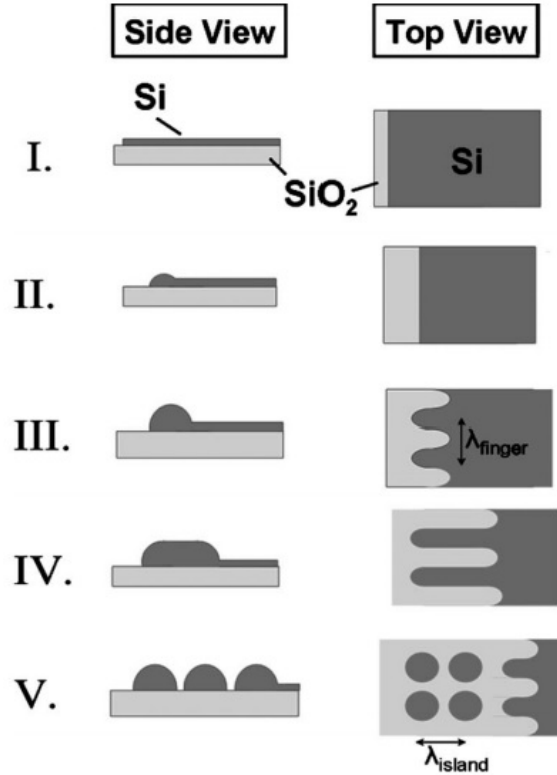
Figure 2.3.   Illustration of the proposed five-step capillarity-driven SOI agglomeration [36].

Further in step four, the high local edge curvature results out flow material which results in pernetration of material forming equally spaced fingers. With the growth of elongated fingers an array of fingers is formed. In the final and fifth step, the long fingers break up into a discrete nanoislands due to the second generalized raileigh instability.

Danielson also studied the relaiton of thickness and the interfacial surface energy dewetting possibilities. To relate the two, first he established a a relation of contact angle which can be dictated by the interfacial surafce tension balance of the depositon (Si) and the substrate (SiO_2), which is given by

$$\theta_c = cos^{-1}\left(\frac{\gamma_{Sub-Dep} - \gamma_{Dep-Sub}}{\gamma_{Dep-vaccum}}\right)$$

Where, $\gamma_{Sub-Deposition}$ is the SiO_2 - vaccum interfacial energ density, $\gamma_{Deposition-Sub}$ is the $SiSiO_2$ interfacial energ density, $\gamma_{Deposition-Vaccum}$ is the Si vaccum interfacial energy density. Figure 2.4 shows the graphic representation of the model used in this study.
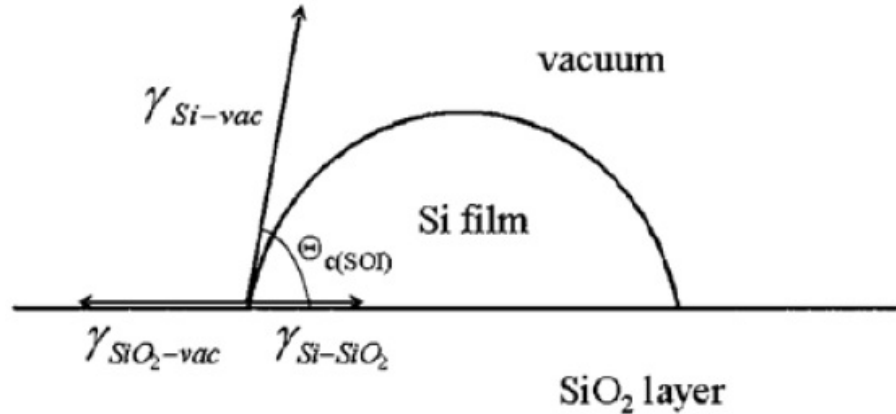
Figure 2.4. Schematics of the model used [36].

Further Danielson et. al established two more relations, out of which first related the change in surface energy and thickness of the deposition and the interfacial surface energies. Second was that of the change in strain which and related the deposition thikness. Below are the equations [36] which obatined.

$$\Delta E_{surfaces} = -\frac{\pi}{3}t_{Si}^2[(13600 * \gamma_{Dep-vaccum}) - (14800 * \{\gamma_{Sub-Dep} - \gamma_{Dep-Sub}\})]$$

$$\Delta E_{strain} = -\frac{\pi}{3}t_{Dep}^3[16000\frac{(1 - v_{Si})\sigma_{Dep}^2}{E_{Dep}}]$$

Where σ_{Dep} the biaxial Si film stress, v_{Dep} is the Poissons ratio, E_{Dep} is the Si elastic modulus, t_{Dep} is the thickness of Si. The schematics of such a model is shown in Figure 2.5.

The significance of the two obtained parameters can be explained by Figure 2.6, which plots Biaxial Si film stress against thickness of deposition indicated by SOI thickness in the figure. The shaded region of the graph represents the surface energy
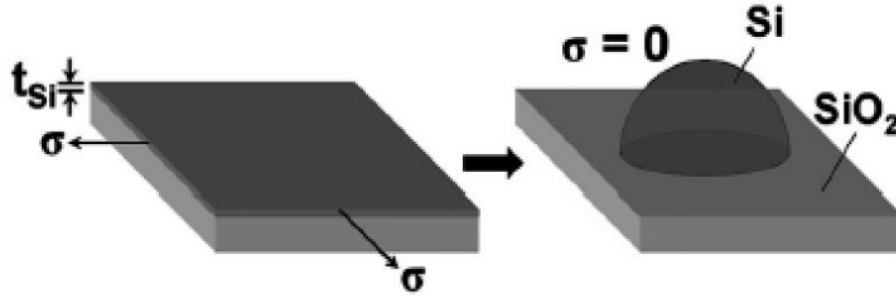
Figure 2.5.   Schematics of the model used for establishing relation between interfacial surface energy and thickness [36].

dominated regime, which is the constraint for the maximum thickness, which can be deposited on the substrate. In this research, the thickness of 30 nm was concluded to be maximum which can be used to restrict to the surface energy driven regime. Another parameter, which can be restricted is that of the biaxial stress, which is restricted to below 100 MPa.

As calculated in this research a relation can be established between thickness and the interfacial surface energy by using contact angle which can estimate the maximum thickness of Au which can be deposited on CNT to restrict the agglomeration face energy dominated regime.

Another important parameter which was calculated in this research was that of the critical radius value of the voids which will not be succumbed by the film and continue to grow with induction of energy. Following equation provides the relation.

$$r_{critical} = \frac{t_{Dep}}{sin\ \theta_c}$$

This relation can be used determine if a void is subcritical which will be succumbed by the film or a supercritical which will grow. This is explained by the schematics shown in Figure 2.7. A supercritical void is expected to grow spontaneously with induction of energy, where as a sub critical void is dominated by the film and is restored by thin film. The void can be generated owing to the crystal originated particles, dislocations, stacking faults and oxide precipitates [38].
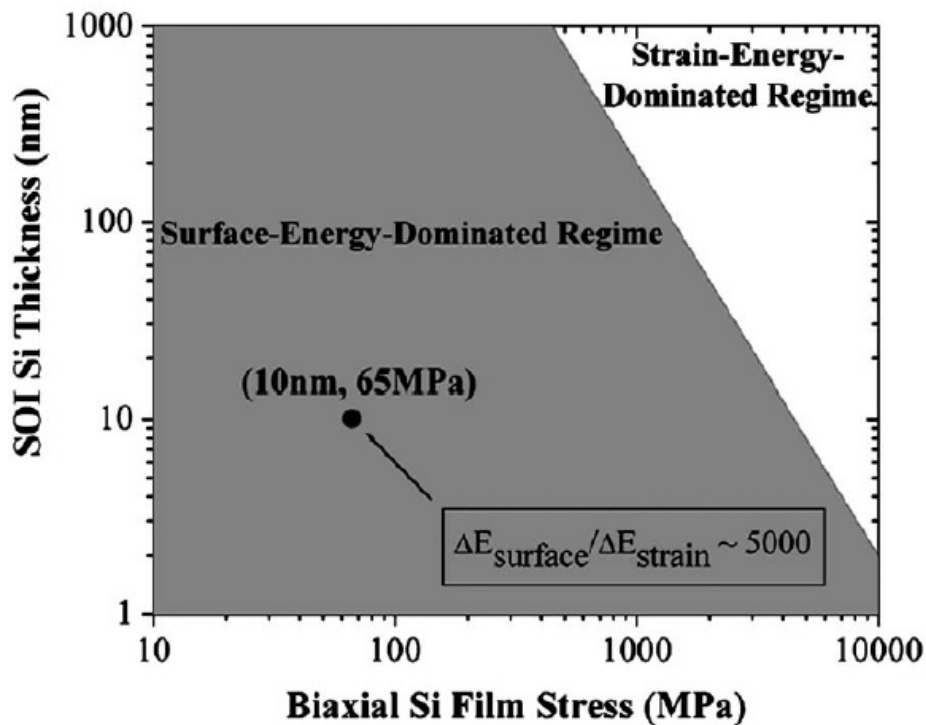
Figure 2.6. Plot indicating regimes of SOI thickness and biaxial Si film stress where surface energy driven reduction (shaded) and strain energy reduction (un-shaded) would dominate during SOI agglomeration [36].
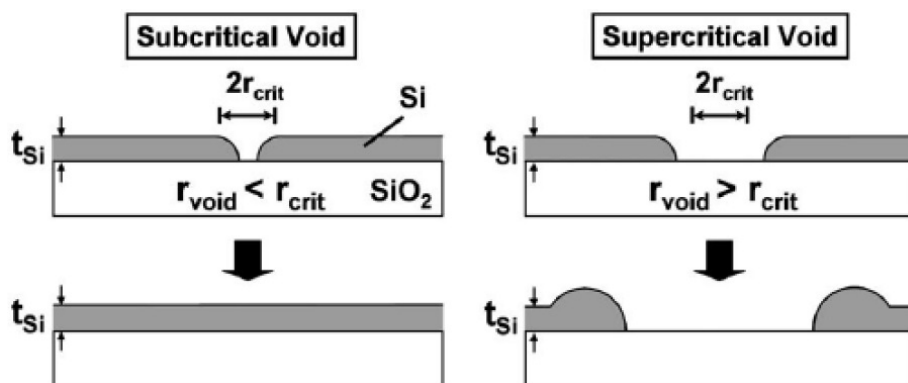
Figure 2.7. Illustration of the critical void phenomenon in agglomeration [36].

Another important parameter which was calculated in this research is that of the nucleation activation energy. The agglomeration initiation that is observed in a flat

film without the defects and edges is due to the nucleation energy. The activation energy can be calculated by the estimating the area of a cylindrical hole with radius magnitude as critical radius and the thickness deposition. The following equation gives the homogeneous void nucleation energy activation energy.

$$\Delta G_{void} = A_{cyl} * \gamma_{Dep-vaccum}$$

$$\Delta G_{void} = 2 * \pi * r_{crit} * t_{Dep} * \gamma_{Dep-vaccum}$$

$$\Delta G_{void} = 2 * \pi * t_{Dep}^2 * \gamma_{Dep-vaccum}$$

2.4   Microscopic Stages of Dewetting

As demonstrated in the earlier section the stages of dewetting of thin film can be observed from the SEM images of gold deposited on CNT. Figure 2.8 SEM images of the various stages of dewetting as observed on the CNT sputtered on gold. First image shows a thin film as sputtered. The film consist of cracks across entire film. The second image is the SEM micrographs of incompletely dewet thin film. The cracks in to larger cracks spreading across the entire sample. Also the CNT fiber are completely exposed in this stage. The next image shows the film into a dewetted stage, although a complete dewetting is not observed at this stage, the elongated finger like structures are seen on the entire sample. The next image is of completely dewetted particles. The particles at this stage are pearled into complete spherical nanoparticles. The next image shows the stage when due to excess energy the particles, within a critical distance undergo Ostwald ripening. Due to the Ostwald ripening the size of the particles grow. On induction of further energy a loss of metal is seen, which results in evaporation of particles and hence the size of the particles is observed to be reducing. This stage is clearly visible in the last image.
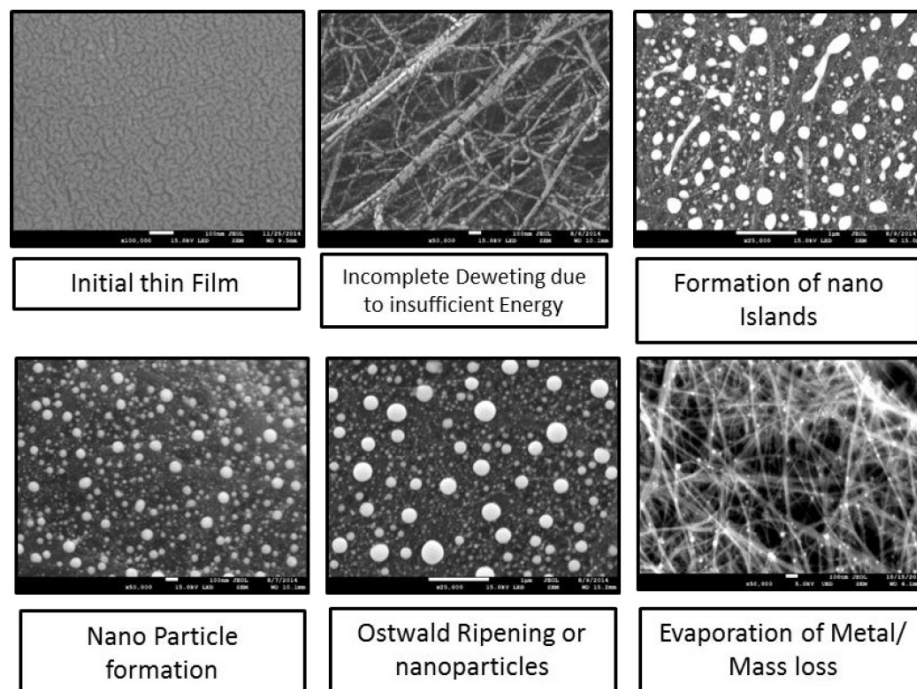
Figure 2.8. SEM images of the various stages of dewetting as observed on the CNT sputtered on gold.

2.5 Energy Source

Energy source is one of necessary factors, which has to be taken into account while considering any technique involving solid state dewetting. Conventional dewetting process involves thermal annealing, for which a furnace can be used. Other sources of energy include, UV irradiation, laser irradiation, electron beam irradiation, ion beam irradiation. Each of these energy sources have their own parameters which account for induced energy density. Such factors need to be taken into account for using these sources.

In this research we have used a xenon flash lamp. The lamp is an intense pulse light capable of producing energy density up to $50 J/cm^2$ and the duration of pulse spans from a millisecond to 10 milliseconds. Use of such a light source facilitates quick one step process involving no cooling or settling time. Also such a source can be used for larger substrates and mass manufacturing involving roll to roll production.

The energy density and duration of pulse restricts heating of substrates, thus the light source proves benign, which means substrates such as polymer and organic compounds can be used.

Intense pulse light is a device which uses flash lamps and computer controlled capacitor bank to generate pulse polychromatic high intensity light. Electrical energy stored in the capacitor is converted into optical energy by passing it through xenon gas within a gas discharge lamp so as to generate bright visible white light. Convertible cut of filter are used to adapt the IPL to a desired wavelength range. Fluence or the energy density of the IPL system is dependent on the voltage which can be controlled.

Figure 2.9.   Image of xenon flash lamp.

Figure 2.9 shows the image of a xenon flash lamp. The lamp has two electrodes at the two ends out of which the cathode is the smaller electrode, which supplies current. The cathode is in the form of a sharp tip which facilitates the emission of electrons. The anode is at the receiving end. The dissipated energy is converted into heat. Only about 80% of the energy is converted into radiation, rest is lost in the form of heat conduction and convection. Out of the 80% only about 50% is radiated from the arc [39], remaining is radiated from the electrode that is anode because of which the lamp temperature rises to 700°C. Such a high temperature makes a water cooling system necessary to be integrated with the lamp.

Such an energy source aligns with our approach and is used in this research.

2.6   Previous Work

2.6.1   IPL Induced Pt NP Formation on CNT

Intense pulse light was used in this research by Ryu, Kim and others, where they demonstrated metal nanoparticle formation [40]. Initial thin film of Pt was sputtered and the IPL irradiation was used to modify the morphology of the thin film. This research demonstrated that the size of nanoparticle could be changed by using the initial thin film thickness. However the size and its relation with other parameters of intense pulse light remained unexplored. As the research was aimed at improving the efficiency of glucose/air biofuel cell, the characterization was mainly done in the energy perspective estimating cell voltage and current density.

2.6.2   IPL Induced Pt-Au Alloy NP Formation on CNT

Another research involving nanoparticle growth on CNTs was done by the same group, where they sputtered layers of two metals namely Pt and Au on CNTs and the layer were treated with IPL irradiation to transforms into nano-islands due to the surface energy driven diffusion [41]. This research aimed at producing nanoparticles of different composition by altering the layer thickness of both Pt and Au. The research aimed at detection of glucose, therefore characterization involved estimation of sensitivity and range of detectable concentration etc. Though use of intense pulse light was done, the parameters affecting dewetting of thin films and nanoparticles formation remained unexplored.

2.6.3   IPL Induced Sintering of Cu Nanoparticles

In this research, the same group used intense pulse light for sintering Cu nanoparticles for use in printer electronics [42]. The simultaneous sintering and reduction of Cu oxide was demonstrated. However the process was in situ reduction of copper

oxide and the existing nanoparticles were worked on. Thus the size and stability were not studied in this research also.

Therefore a void remained, questioning the relationship of parameters of intense pulse light and the factors affecting the dewetting. In this research we have tried to put light on the subject, and studied the details of dewetting process. One of the major concerns was of the stability of the nanoparticles and the ability of the intense pulse light to produce thermodynamically stabilized nanoparticles. Another major question was that can control over size of nanoparticles be achieved in such a technique. We have tried to address these issues in our research.

2.7 Thesis Objective

The primary objective of the thesis is to demonstrate the technique of use of intense pulsed light for dewetting of thin film. An Au layer of thickness ranging from 3 nm to 30 nm is sputtered on CNTs. The sputtered film is to be then converted in to thermodynamically stable nanoparticles.

Second major objective of the thesis is to prove the control over the size and stability of particles. The research experimentally, tries to develop a relation between various factors affecting solid state dewetting process.

Optimization of the parameters of xenon lamp is to another objective. Parameters of induced energy density, number of pulse, duration of pulse and the duration of gap whenever multiple pulse are used need to be constrained. And a scheme can be developed to arrive at a particular result. The thesis aims as providing such a scheme.

Thermodynamic stability of the particles is to be confirmed so that the hypothesis can be proved. Experiments are also carried and demonstrated to confirm the same.

Also it is very essential to compare the proposed technique with a conventional method. The later part of the research tries to compare and account the parameters for comparison between xenon flash induced solid state dewetting and conventional thermal dewetting process to check the precision and reliability.

3. EXPERIMENTAL DETAILS

This chapter explains the experimental details, which includes the detailed procedure of sample preparation, apparatus used for experimenting and characterizing the sample. Also the design of experiments is focused and every set of experiment with its objective is explained.

3.1 Sample Preparation

CNT mat provided by *NanoComp* Technologies, Inc. CNTs are available in various forms. The CNT provided to us was in form of a matrix, which was a sheet or a mat. The CNT mat is a sheet of multi-walled CNTs, whose length and diameter are about 1 to 3 mm and 40 nm to 100 nm, respectively. The average thickness is measured to be 12 um. The mat was cut into 5 mm x 5 mm pieces to mount them on a silicon wafer. Silicon wafer was also cut into pieces. Each piece was cut about 1 cm x 1 cm. Silicon wafer was used as a base so as to hold the delicate mat of CNT. It wholly served as a platform to assist transfer and handling and samples. The use of silicon wafer does not affect or bias the results of the experiments. Once the silicon wafer was cut, the small piece of CNT mat was mounted on the silicon wafer. To adhere it well on the wafer. The edges were stretched and pressed. The adhering was sufficient to hold the CNT and prevent it from peeling of the silicon wafer during sputtering, annealing or characterizing.

Figure 3.1 show the image of the sample ready to be treated. Once the sample was ready, it was sputtered with Au to form a thin film on the CNT. 3 nm, 6 nm, 9 nm, 15 nm, and 30 nm of Au thin-films were deposited on to the CNT mat using magnetron sputtering technique. The base pressure of the system was about 10^{-8} torr. The Ar pressure and DC power were 4Pa and 50W, respectively. Sputter rate was calculated
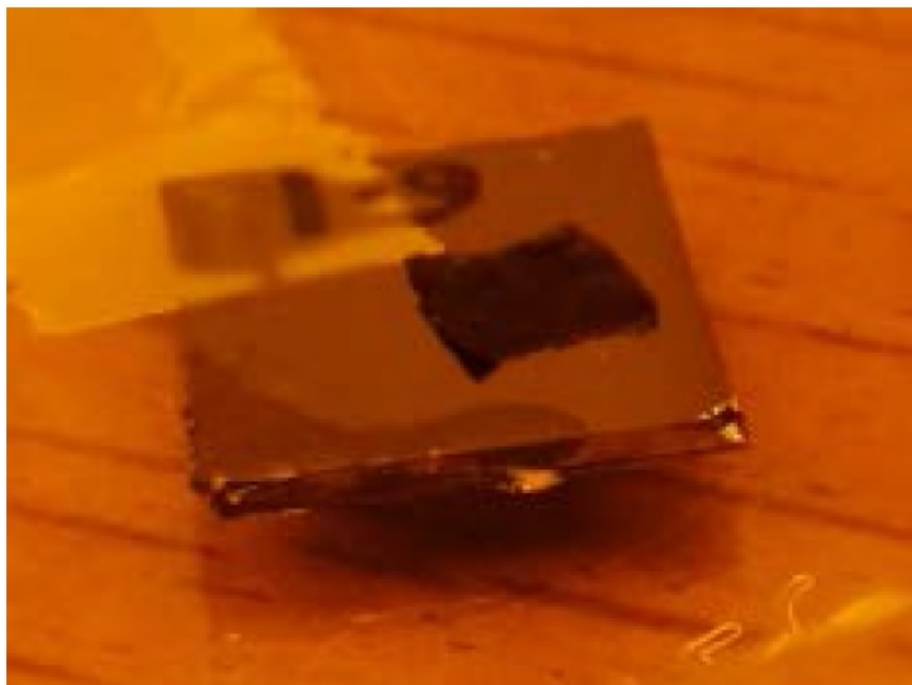
Figure 3.1. Image of sample.

by linear interpolation. A 30 seconds sputtering time deposited a 9 nm of thin film, which was measured using Atomic force microscope. With this calculation the rate was found to be 3Å/s. Another measurement was done for 60 seconds to confirm this rate.

Annealing was done using two methods:

1. Xenon flash lamp annealing

2. Conventional thermal furnace annealing

Xenon flash annealing is process of annealing samples. It consists of flashing an intense pulsed light on the sample. The energy is induced by radiation and selectively heats the Au metal deposited on the CNT. The selective heating done in millionth of a second causes the metal film to dewet into nanoparticles. The details of the process are explained in the further articles.

Conventional annealing process consists of heating sample to high temperature in an electric furnace for longer time duration. The heating temperature depends on the thickness of the Au film deposited. Duration is also dependent on the film thickness. It usually ranges between 1 h to 4 h period, after which the furnace has to be left to cool down to room temperature before the sample can be pulled out. The details of this process are also explained in further articles.

Figure 3.2 shows the experimental arrangement of xenon annealing setup. The image shows the cable, which delivers power and also serves as the tubing for water cooling system. The lamp head houses the xenon lamp. The sample is placed on stage which can be moved in Z-direction so as to change the distance between the lamp and the sample, which is referred to as working distance.
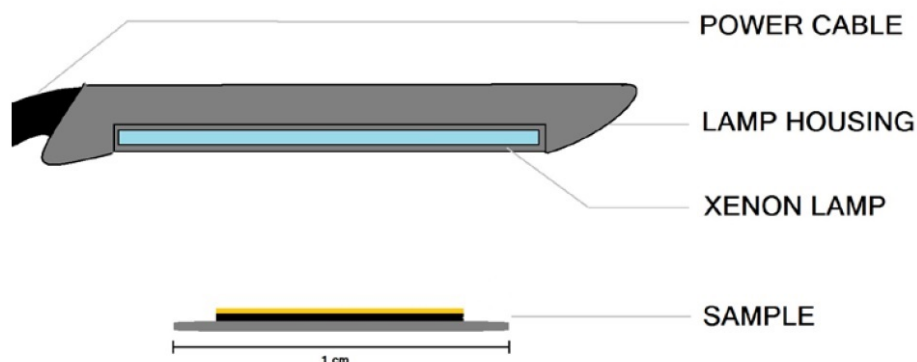
Figure 3.2. Arrangement of experimental setup for xenon flash annealing.

The next step is of characterization of the samples which is done using electron microscope. High resolution images of about 200K to 300 K are obtained. Once the images are obtained, they are tuned in Photoshop so that, particles are significantly brighter that the background. The tuned image can then be analyzed with ImageJ. ImageJ is a software which can analyze an SEM image. The software recognizes the particles which are brighter and accounts for pixels. The pixels are then converted into area units using a set scale which depends on the magnification of the SEM image. Area obtained of every particle is then converted to obtain diameter, for which every

particle is considered circular. The accounted particles are then statistically analyzed using Microsoft excel.

3.2   Apparatus

The Xe-lamp used in this research has 20 mm arc length. The linear Xe-lamp housing has a wide window of 30 mm x 10 mm, and the lamp is cooled by water that circulates around the lamp tube and the housing. Xe gas converts nearly 50% of electrical energy into radiation energy [39]. The Intense pulse light system is a commercial skin rejuvenating hair removal machine which can ionize Xe gas to generate up to 50 J/cm^2 of flash energy density. The power supply and trigger circuit are designed to deliver up to 15 flashes per trigger with a maximum trigger rate of 1Hz. Flash duration and delay between flashes can be adjusted between 0.5 ms to 30 ms and 1 ms to 10 ms, respectively.

Figure 3.3 shows the image of the xenon flash lamp used for experiments, the system consist of the lamp holder which houses the xenon arc and the water cooling arrangement. The lamp head is connected to the electrical unit. The electrical unit contains an HMI to adjust the parameters of the lamp.

Thermal annealed control samples are prepared by a high temperature furnace (*Thermo Scientific*, FB1315M). The evolution and coalescence of nanoparticles by Xe-flash are observed by SEM (*JEOL* JSM-7800F).

3.3   Design of Experiments

A standard condition was obtained with the input energy of 50 J/cm^2, with a 2 ms duration pulse and a single flash of intense light. The working distance between lamp head and sample was maintained at 1 cm.

Figure 3.3. Image of commercial xenon flash lamp used in the study.

3.3.1 Preliminary Experiments

First set of experiments aimed at estimating the trend with change of parameters. Following experiments were done in this set:

1. Sensitivity to energy: 10 J/cm^2, 25 J/cm^2, 50 J/cm^2

2. Sensitivity to number of pulse: 1, 3, 6

3. Sensitivity to gap duration: 2 ms, 5 ms, 10 ms

4. Sensitivity to pulse duration: 2 ms, 5 ms, 10 ms

5. Sensitivity to thickness of film: 3 nm, 6 nm, 9 nm, 15 nm, 30 nm

3.3.2 Minimum Dewetting Energy Estimation

Once the trend was estimated. Second set of experiments aimed at calculating a minimum dewetting energy for a particular thickness. Three samples were used for this set of experiments. For every thickness value sample, increasing energy pulses were flashed. Energy was increased for 5 J/cm^2 to 50 J/cm^2, with an increment of 5 J/cm^2. The experiment was stopped when complete spherical nanoparticles were obtained. Experiments were done for following thickness samples:

1. 3 nm

2. 6 nm

3. 9 nm

3.3.3 Evaporation Point Estimation

Third set of experiments were done to check the evaporation energy of the samples. These experiments aimed at estimating the energy at which mass loss was observed and evaporation of metal was confirmed. Following experiments were done to check the evaporation point.

1. 3 nm

2. 6 nm

3. 9 nm

3.3.4 Dewetting using Multiple Pulse

Fourth set of experiments aimed at samples with higher value of thickness for which energy variation or the highest amount of energy of 50 J/cm^2 was not sufficient enough to transform the deposition into spherical nanoparticles. In such a condition multiple pulse were used with an energy gap of 2 ms between every flash. Consecutive

pulse were increased one flash at a time and were increased until complete spherical nanoparticles were obtained. Following experiments were done to check the feasibility of this method:

1. 15 nm

2. 30 nm

3.3.5 Confirmation of Thermodynamic Stability

Fifth set of experiments aimed at checking the thermodynamic stability of nanoparticles. The already dewetted samples were flashed with the same energy magnitude and the sample was characterized to observe for any changes in size or evaporation. Such flashing was repeated for 5 times and analyzed after every shot. Following experiments were done to confirm thermodynamic stability

1. 6 nm

2. 9 nm

3.3.6 Conventional Thermal Annealing Method

Sixth set of experiments were done to compare the two annealing methods. So far the flash annealing was completed and conventional furnace annealing experiments were to be designed. For comparison purpose samples were annealed in furnace. Until spherical nanoparticles were formed. A starting temperature of 100°Cwas used and annealing time was increased from 1 h to 4 h with an increment of 1 h at a time. Duration was increased until 4 h, after which temperature was increased to 200°Cand again time duration was taken from 1 h to 4 h. Such iteration were continued until complete spherical nanoparticles were observed within 4 h of duration. To check the thermodynamic stability of this method extended duration time was used. Temperature of complete annealing was maintained for 6 h and 10 h periods

and samples were annealed. Samples were then characterized to check the change in size. Once the change in size was confirmed to be negligible the conventionally annealed sample were compared to the flash annealed samples. Following experiments were used to compare the two methods:

1. 6 nm

2. 9 nm

4. RESULTS

This chapter enlists the results obtained from the experiments discussed in the above chapter. All the experimentally obtained parameters such as the size of particles and the standard deviation are stated. Also the trends of the results are compared by visual observation and the SEM images are added wherever required.

4.1 Preliminary Results

Preliminary results consisted of the first set of experiments aimed at determining the trend of following parameters of xenon flash lamp.

1. Energy input

2. Number of pulse

3. Duration of pulse

4. Duration of gap between pulse

5. Thickness of initial thin films.

Variation of energy experiment was done with a 9 nm initial thin film, three iteration were done with energies of 10 J/cm^2, 25 J/cm^2 and 50 J/cm^2. Pulse duration was maintained at 2 ms, only a single flash was used and the working distance was maintained of 1 cm. The energy variation showed increasing size of nanoparticles as observed visually in Figure 4.1.

Next experiment consisted of variation of number of pulse. As in previous experiments, 9 nm initial thickness was used. A 50J energy was used, duration of pulse and gap duration was maintained of 2 ms. Working distance on 1 cm was maintained at all times. Three iteration were done of 1, 3, 6 consecutive pulses. Increasing number
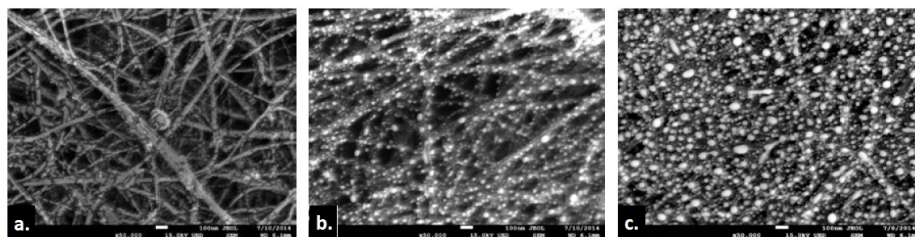
Figure 4.1. SEM Image of 9 nm sample treated with (a) 10 J/cm^2, (b) 25 J/cm^2, (c) 50 J/cm^2.

of pulse showed initial increase in the size of NPs but size decreased when the 6 pulses were flashed as visually observed in Figure 4.2.
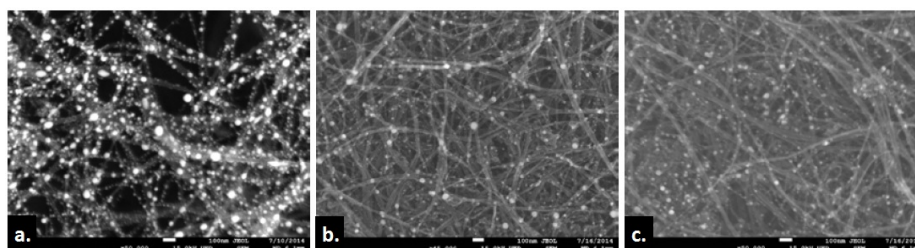

Figure 4.2. SEM Image of 9 nm samples treated with (a) 1, (b) 2, (c) 3 consecutive pulse.

Variation of pulse duration was performed with a 9 nm initial film thickness, with energy of 50 J/cm^2. A single pulse was flashed. Duration of the pulse was varied. 2 ms, 5 ms and 10 ms of time was used. Working distance on 1 cm was maintained at all times. Increasing pulse duration showed a steady, almost linear decrease of size of NPs as visually observed in Figure 4.3.

Next set consisted of variation of duration of gap between pulses. A 9 nm initial thin film sample was used, with energy of 50 J/cm^2 and 3 consecutive flashes were used. Duration of pulse was maintained at 2 ms and working distance on 1 cm was maintained at all times. The variation of gap duration showed initial decrease in size but then the size increased as the gap duration was increases to 10 ms as visually observed in Figure 4.4.
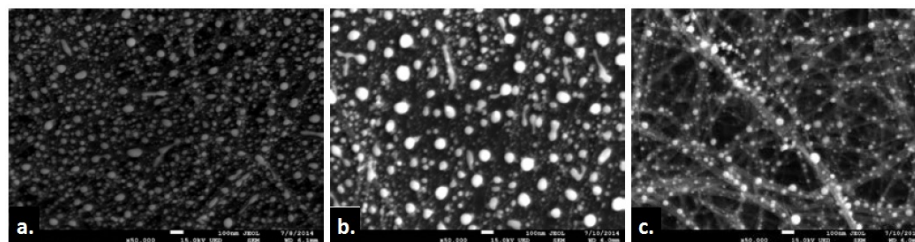
Figure 4.3. SEM Images of samples treated with (a) 2 ms, (b) 5 ms, (c) 10 ms of pulse duration.
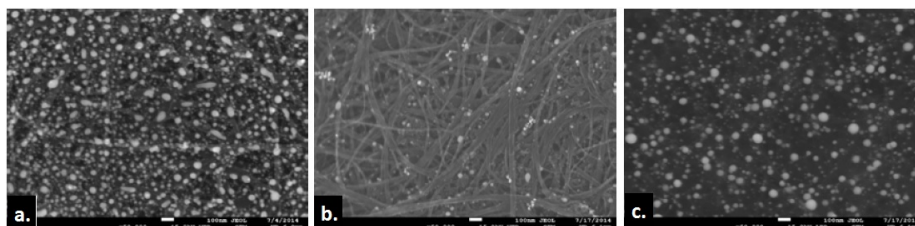

Figure 4.4. SEM Images of samples treated with (a) 2 ms, (b) 5 ms, (c) 10 ms of gap duration.

Variation of thickness was the final experiment, where samples of 6 nm, 9 nm, and 15 nm and 30 nm samples were used. 50 J/cm^2 of energy input with 2 ms pulse and gap duration was used. Working distance on 1 cm was maintained at all times. The trend shows that the lower thickness sample showed complete spherical NPs formation but as the thickness increased the size and standard deviation of particles increased as visually observed in Figure 4.5.
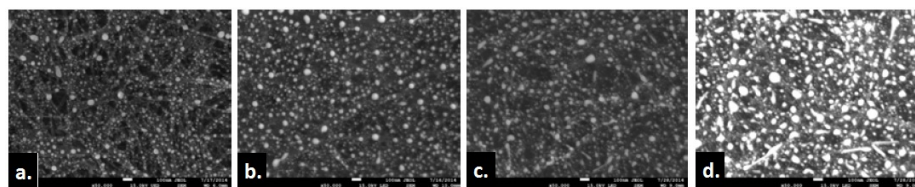

Figure 4.5. SEM images of (a) 6 nm, (b) 9 nm, (c) 15 nm, (d) 30 nm samples treated with 50 J/cm^2 single pulse.

4.2 Minimum Dewetting Energy

The next set of experiments were done to estimate the minimum dewetting energy. A single pulse of Xe-Flash was applied with increasing energy densities from 5 J/cm^2 to 50 J/cm^2, with an increment of 5 J/cm^2 were applied to samples of 3 nm, 6 nm, 9 nm, 15 nm, 30 nm of Au deposition on CNT matrix.

As predicted by the Volmer-Webber model, a 3 nm deposition was in form of irregular nano-islands as shown in Figure 4.6.
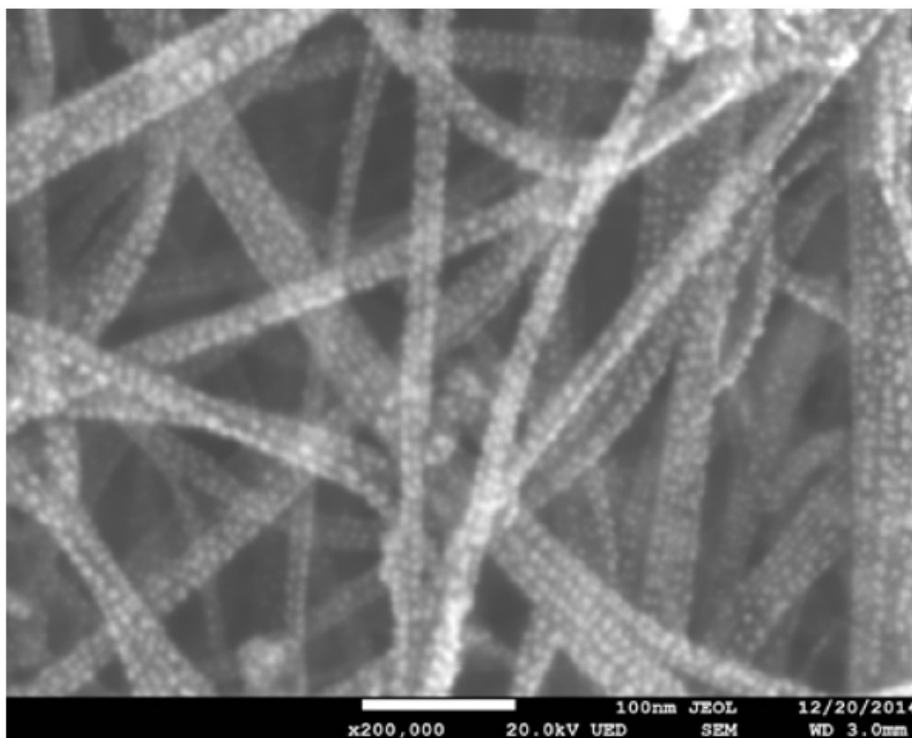
Figure 4.6. SEM image of an untreated 3 nm sample showing irregular nano-islands.

With an induction of 5 J/cm^2 from the Xe-flash the irregular nano-islands are pearled into spherical nanoparticles as shown in Figure 4.7. Average size and standard deviation of nanoparticles was measured to be 6.12 nm and 2.21 respectively. Upon induction of 10 J/cm^2 of energy density the nanoparticle size grew to 7.89 nm with a standard deviation of 2.91.
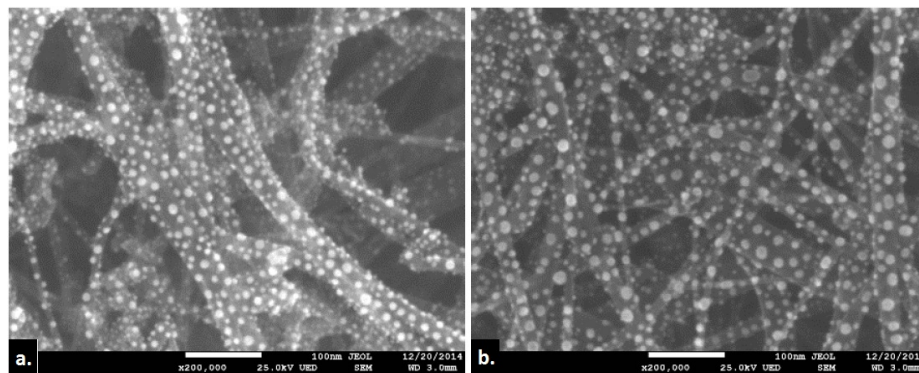
Figure 4.7. (a) SEM image of 3 nm deposition treated with a single pulse of 5 J/cm^2 energy density. (b) SEM image of 3 nm deposition treated with a single pulse of 10 J/cm^2 energy density.

The increase in size of nanoparticle is due to the coalition of particles within a critical diffusion length of Au on CNTs [34, 35]. The size growth seizes between the 10 J/cm^2 to 20 J/cm^2 which marks complete nanoparticle formation.

In case of 6 nm and 9 nm deposition, a continuous thin film is observed instead of irregular nano-islands as shown in Figure 4.8.
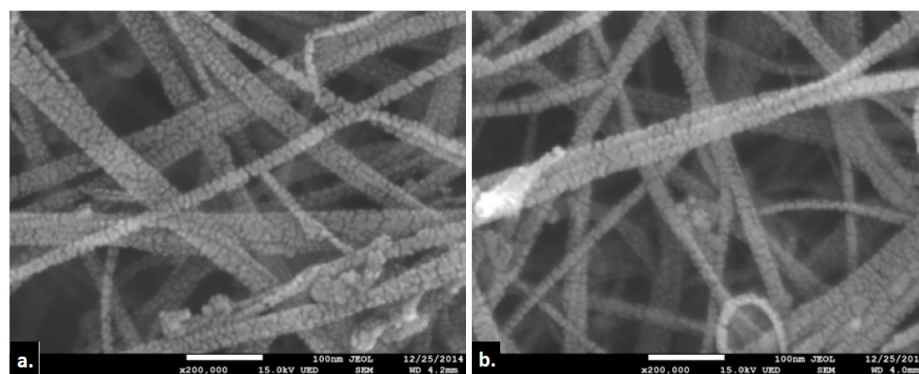

Figure 4.8. SEM image of an untreated (a) 6 nm and (b) 9 nm sample.

Energy density of 5 J/cm^2, 10 J/cm^2 and 15 J/cm^2 proved to be insufficient for formation of spherical nanoparticles. However with an increased energy density of 20 J/cm^2 and 35 J/cm^2 was sufficient enough to transform the film into spherical nanoparticles, of a 6 nm and 9 nm deposition as shown in Figure 4.9.
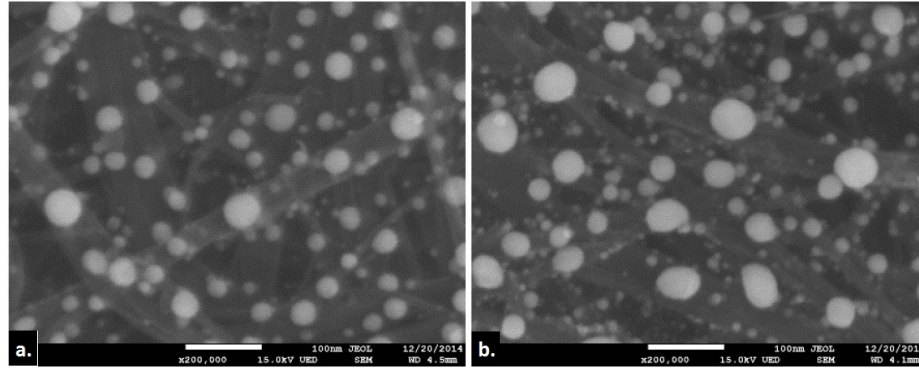
Figure 4.9. (a) SEM image of (a) 6 nm sample treated with a single pulse of 20 J/cm^2 energy density and (b) 9 nm sample treated with 35 J/cm^2 of energy density.

4.3 Evaporation Point

Similar experiments were done to estimate the evaporation point. For this set of experiments 3 nm, 6 nm and 9 nm samples were used. On further increment of induced energy density that is from 25 J/cm^2, a reduction in size of nanoparticles is observed for 3 nm. The excess energy induction significantly reduces the average size of nanoparticles of a 3 nm film as observed in the case of 50 J/cm^2 sample where the average size and standard deviation of particles are found to be 5.4 nm and 2.38 respectively.

Experiments were also conducted so as to estimate evaporation point for both 6 nm and 9 nm initial thin film. Evaporation and reduction in size was observed at 50 J/cm^2 for both the samples.

We hypothesized that the coalition of nano-islands within the diffusion length and the evaporation responsible for size reduction occur concurrently. The larger size of nanoparticle post the Xe-flash treatment Figure 4.10 as compared to the initial nano-islands Figure 4.7 befits the hypothesis.

The incomplete dewetting stages showed transformation of continuous film into elongated finger like structures until they were completely transformed into spherical nanoparticle which is shown in Figure 4.11.
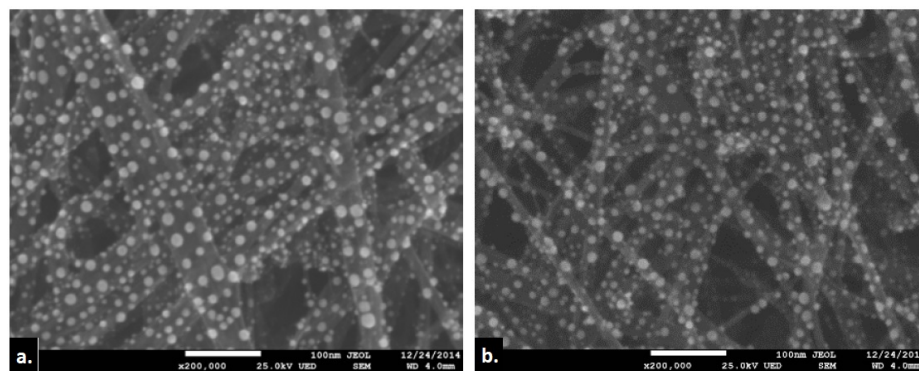
Figure 4.10. SEM image of 3 nm deposition treated with a single pulse of (a) 25 J/cm^2 and (b) 50 J/cm^2 energy density showing reduction of particles due to evaporation.

Figure 4.11. SEM image of 9 nm deposition treated with a single pulse of 10 J/cm^2 energy density.

The average size of the completely dewetted nanoparticles were found to be 12.91 nm and 22.31 nm, whereas the standard deviation for the sizes were found to be 1.67

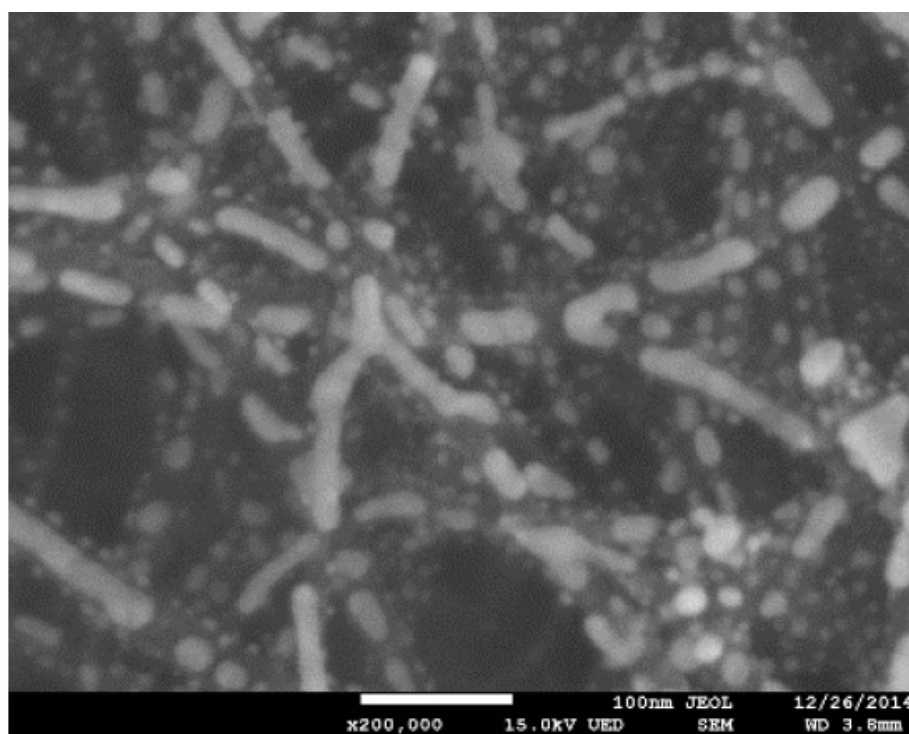and 13.43. On induction of excess energy, that is more than the minimum required energy, particles showed evaporation of nanoparticles as shown in Figure 4.12.
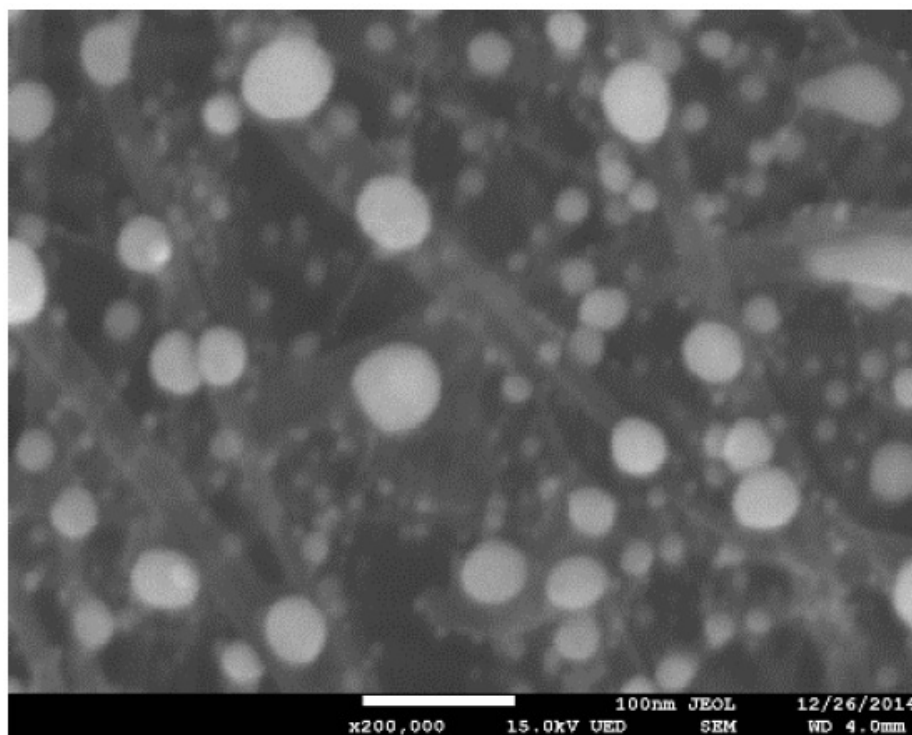
Figure 4.12. SEM image of 9 nm deposition treated with a single pulse of 50 J/cm^2 energy density.

4.4   Dewetting Using Multiple Pulse

In case of 15 nm and 30 nm deposition the maximum induced energy of 50 J/cm^2 is observed to be insufficient as shown in Figure 4.13. To transform the film into completely dewetted nanoparticles we chose to treat the samples with multiple exposures of 50 J/cm^2 with a duration on 2 ms, until complete transformation of film into spherical nanoparticles occurred.

After 3 and 4 consecutive pulses for 15 nm and 30 nm depositions spherical nanoparticles were observed which is shown in Figure 4.14. It should be noted that the size range of nanoparticles was significantly wider as compared to the ranges of 3
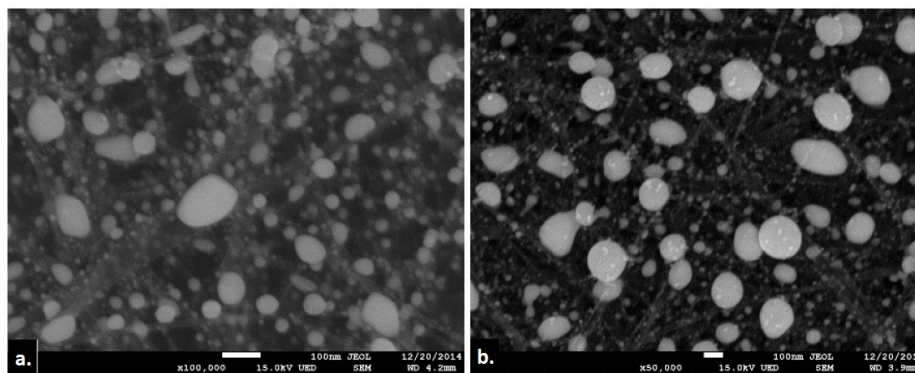
Figure 4.13. SEM image of (a) 15 nm and (b) 30 nm sample treated with a single pulse of 50 J/cm^2 energy density.

nm, 6 nm and 9 nm. The phenomenon of Ostwald ripening occurring during or after dewetting may be the reason for such an irregularity [8].
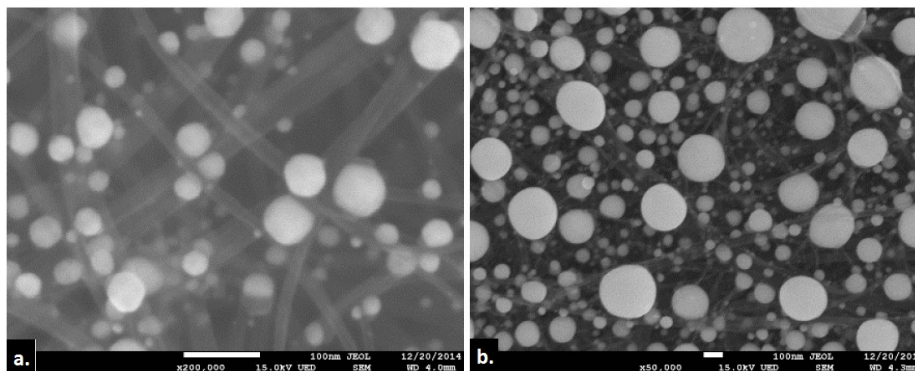
Figure 4.14. SEM image of (a) 15 nm sample treated with 3 pulses of 50 J/cm^2 energy density and (b) 30 nm sample treated with 4 pulse of 50 J/cm^2.

4.5 Confirmation of Thermodynamic Stability

Further the minimum energy density of 10 J/cm^2, 20 J/cm^2 and 35 J/cm^2 were used to check the thermodynamic stability of the sample of 3 nm, 6 nm and 9 nm respectively. We exposed completely formed nanoparticles of 3 nm, 6 nm, 9 nm at

$10 \ J/cm^2$, $20 \ J/cm^2$ and $35 \ J/cm^2$, respectively to another flash to check for any changes in the size. Such checks was repeated 5 times and no significant change was observed in the sizes of the particle sizes as shown in Figure 4.15 for 6 nm and Figure 4.16 for 9 nm respectively.

Figure 4.15. SEM images of 5 stability checks of 6 nm sample treated with a single pulse of $20 \ J/cm^2$ energy density.
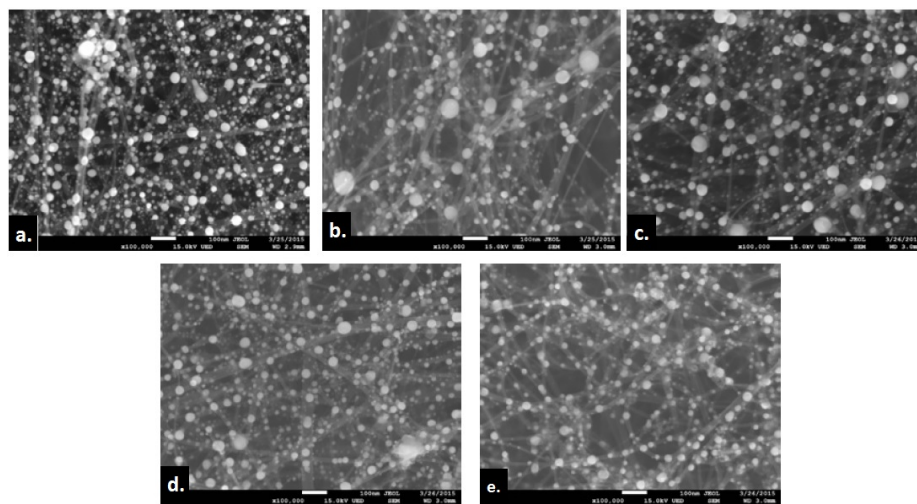
Figure 4.16. SEM images of 5 stability checks of 9 nm sample treated with a single pulse of $35 \ J/cm^2$ energy density.

4.6 Conventional Thermal Annealing Method

For comparison of the two methods of dewetting, it was necessary to obtain the average sizes and standard deviation by con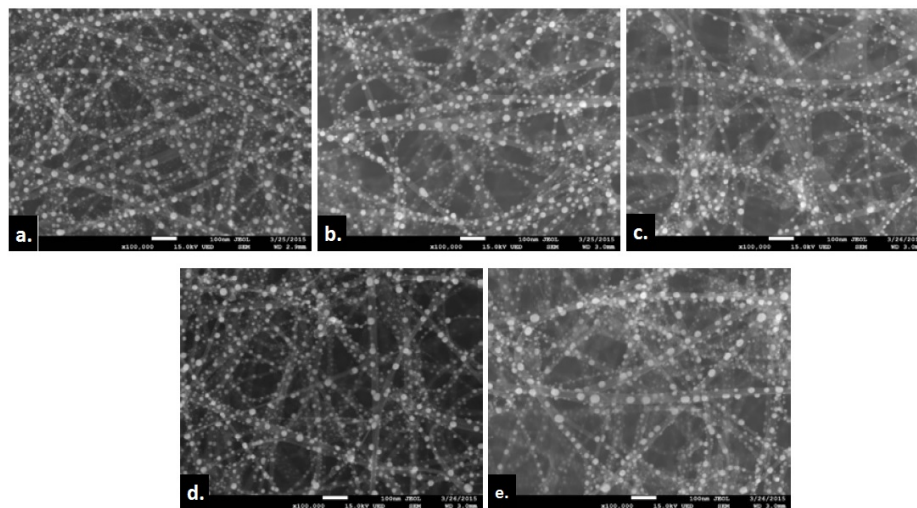ventional thermal annealing methods. 6 nm sample was annealed for 1 h, 2 h, 3 h, and 4 h period at 100°C. Complete dewetting was not observed, hence temperature was raised to 200°C and the four time periods were repeated. Temperature was further raised to 300°C with same time periods of annealing time.

Figure 4.17 shows the SEM images of the 6 nm deposition annealed at 100°C, where the film does no dewet into particles. However the cracks are observed across the entire sample which widen even after annealing time is increased to 4 h.
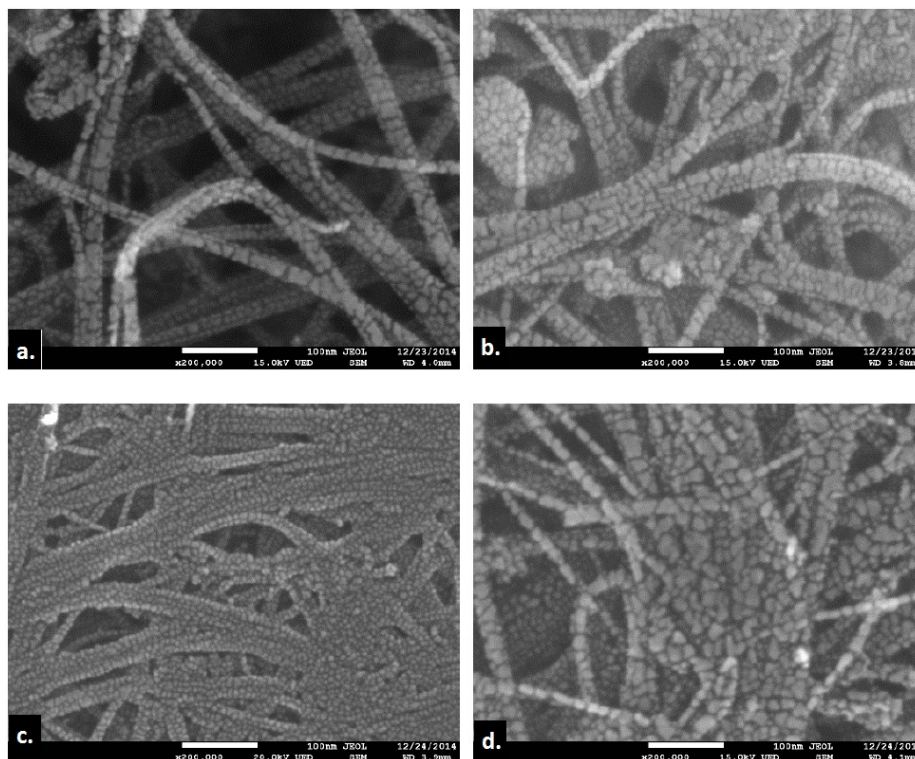
Figure 4.17. SEM results of the undewetted film with annealed at 100°C for (a) 1 h, (b) 2 h, (c) 3 h, (d) 4 h respectively.

Similarly, an experiment was done for the same 6 nm deposition and annealed with 200°C, this sample showed nanoparticles formation which were not in a complete

dewetting stage. Long elongated structure were observed across the entire sample but pearled spherical nanoparticles were not populated as seen in Figure 4.18.
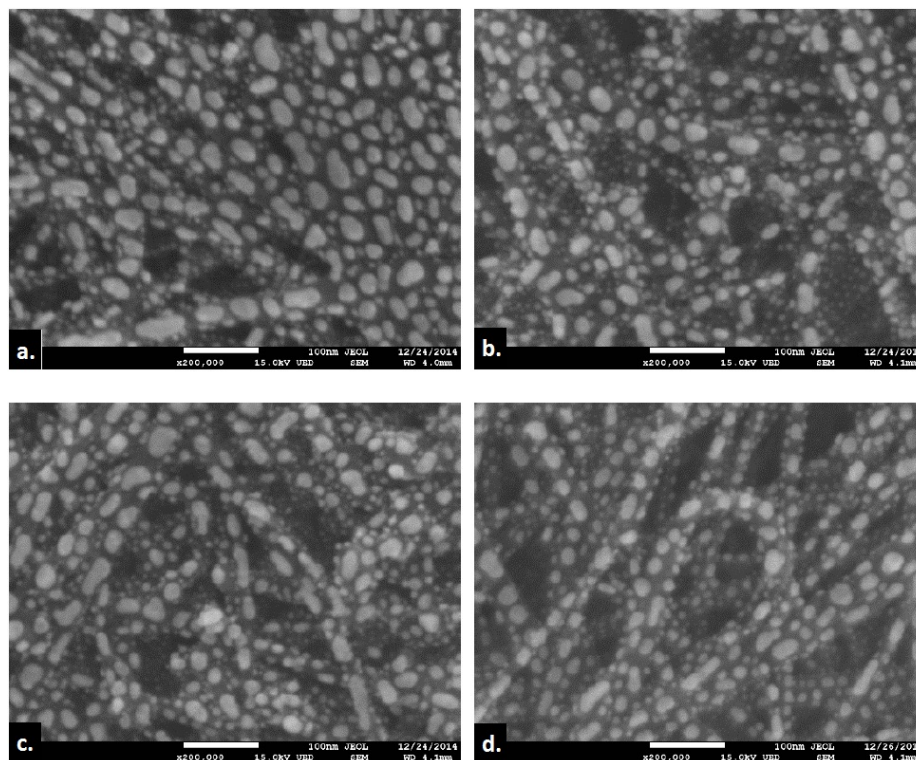
Figure 4.18. SEM results of the undewetted film with annealed at 200°C   for (a) 1 h, (b) 2 h, (c) 3 h, (d) 4 h respectively.

Complete nanoparticle formation was observed with the 4 h annealed sample at 300°C.

To confirm the stability, the annealing time was increased to 6 h and 10 h long period. The average size of the 4 h, 6 h and 10 h was found to be 14.42 nm, 15.11 nm, and 14.74 nm respectively, which give a standard deviation of 0.74. Figure 4.19 provides the visual confirmation for the stability of particles for 6 nm annealed at 300°C for 4 h, 6 h, and 10 h.

Experiments were also done to check the dewetting on a 9 nm deposition, from the experiments of 6 nm deposition it was clear that the temperature of 100°C   and

Figure 4.19.   SEM images of 6 nm thermally annealed at 300°C
sample for (a) 4 h, (b) 6 h, and (d) 10 h of annealing times.

200°C were insufficient to dewet a 6 nm deposition, hence the 9 nm deposition would
require a higher temperature.

Figure 4.20.   SEM images of 9 nm thermally annealed at 300°C
sample for (a) 4 h, (b) 6 h, and (c) 10 h of annealing times.

Hence experiment was done at 30°C annealing temperature and the annealing
duration was increased from 1 h to 4 h with an increment of an h. The Figure 4.20

shows the SEM results of a 9 nm deposition annealed at 300°C for 1 h, 2 h, 3 h, and 4 h respectively.

Form the above results it was clear that the 9 nm sample could not be dewetted in to particles with an anneling temperature of 300°C. Hence temperature was further raised to 400°C and experiments were conducted.

A 9 nm sample was treated until complete nanoparticle formation was observed, which was at 400°C for a period of 4 h. The thermodynamic stability was checked by annealing the sample for extended 6 h and 10 h. The average size for 4 h, 6 h and 10 h was found to be 20.67 nm, 22.51 nm and 22.84 nm respectively, which gave a standard deviation of 1.16. Figure 4.21 shows the particles obtained at 400°C after 4 h, 6 h and 10 h of annealing time.
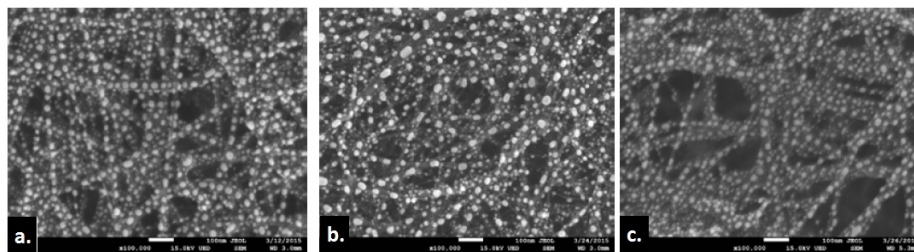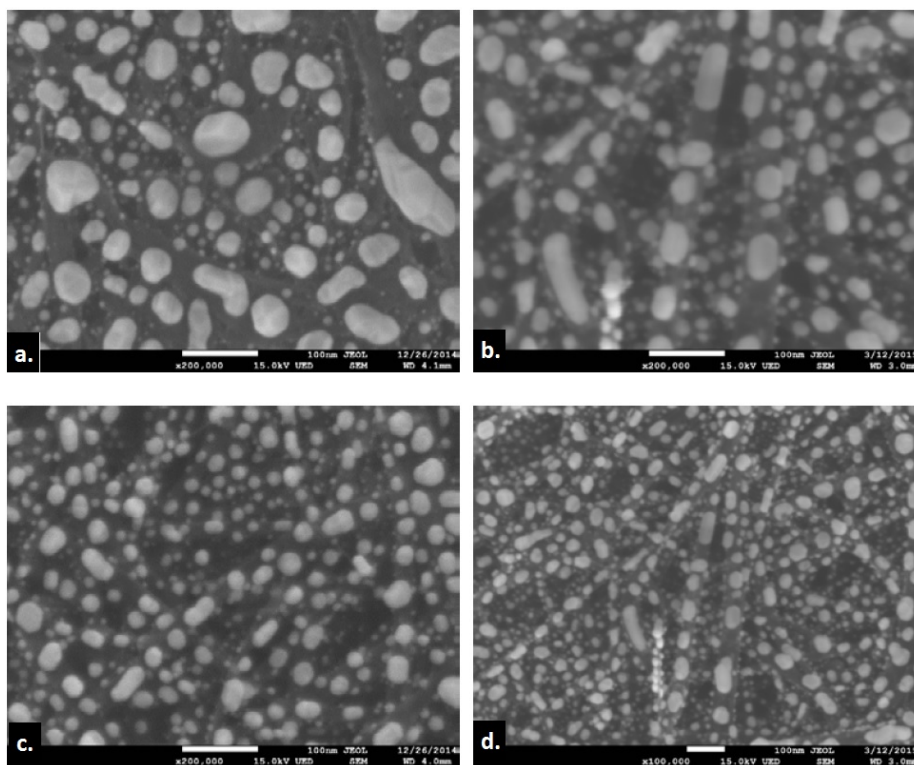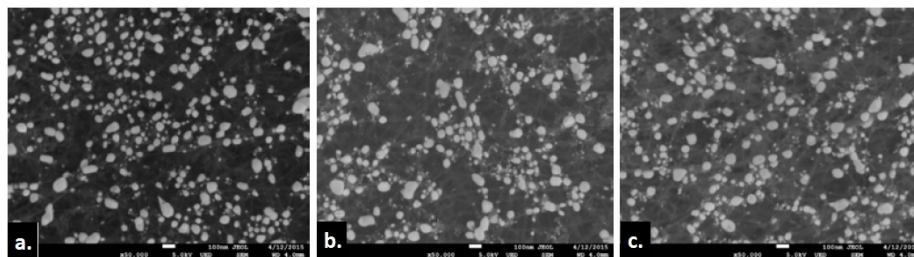

Figure 4.21. SEM images of 9 nm thermally annealed sample for (a) 4 h, (b) 6 h, and (c) 10 h of annealing times.

Before concluding the annealing temperatures, experiments were also conducted with a temperature above the obtained temperature for 6 nm that is 300°C and for 9 nm that is 400°C. The use of higher temperatures resulted in undesirable crystallization of nanoparticles. The nanoparticles at this stage underwent a morphology change and developed edges as seen in Figure 4.22.
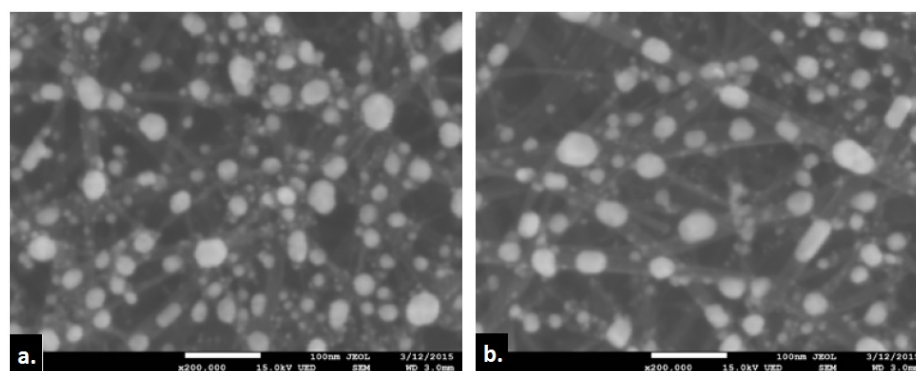
Figure 4.22. SEM results for thermal annealed experiments carried at higher temperature showing edge formation of particles. (a) 6 nm deposition annealed at 400°C for an hour (b) 9 nm deposition annealed at 500°C for an hour.

5. DISCUSSION

This chapter contains a detailed discussion of the obtained results. Trends observed are discussed with supporting theory. Also the analyzed results are compared to theoretically obtained values so as to confirm the hypothesis.

5.1   3 nm

The size of dewetted droplet in thermodynamic equilibrium is proportional to $h^{(1.54\pm0.08)}$, where h is the initial thickness of thin-film [31].With this equation a 3 nm film gets transformed into particles ranging from 4.97 nm to 5.93 nm. The theoretical value calculated shows average diameter to be 7.89 nm at complete dewetting configuration of 10 J/cm^2. It is to be noted that the irregular nano-islands are pearled into spherical nanoparticles of size 6.12 nm with 5 J/cm^2 of energy input. As mentioned above with 10 J/cm^2 the size becomes 7.89 nm and this size remains fairly constant if 25 J/cm^2 energy is used instead of 10 J/cm^2. However the size reduces if more than 25 J/cm^2 of energy is used, as observed when the 50 J/cm^2 pulse is used which gives an average diameter of 5.41 nm. Thus it can be concluded that the complete particle formation requires 10 J/cm^2 of energy for an initial 3 nm Au deposition. It can also be said that the coalition of irregular nano-islands continues to occur until minimum dewetting energy is used, which is a function of initial film thickness. Also evaporation of metal occurs if energy greater than the minimum dewetting energy is used.

Thus the evaporation energy can also be considered function of the initial film thickness. The distribution charts in Figure 5.1 confirms these two processes.

When a 5 J/cm^2 of pulse is flashed the irregular nano-islands diffuse to pearl into spherical nanoparticles. The distribution of nanoparticles obtained equally suggest
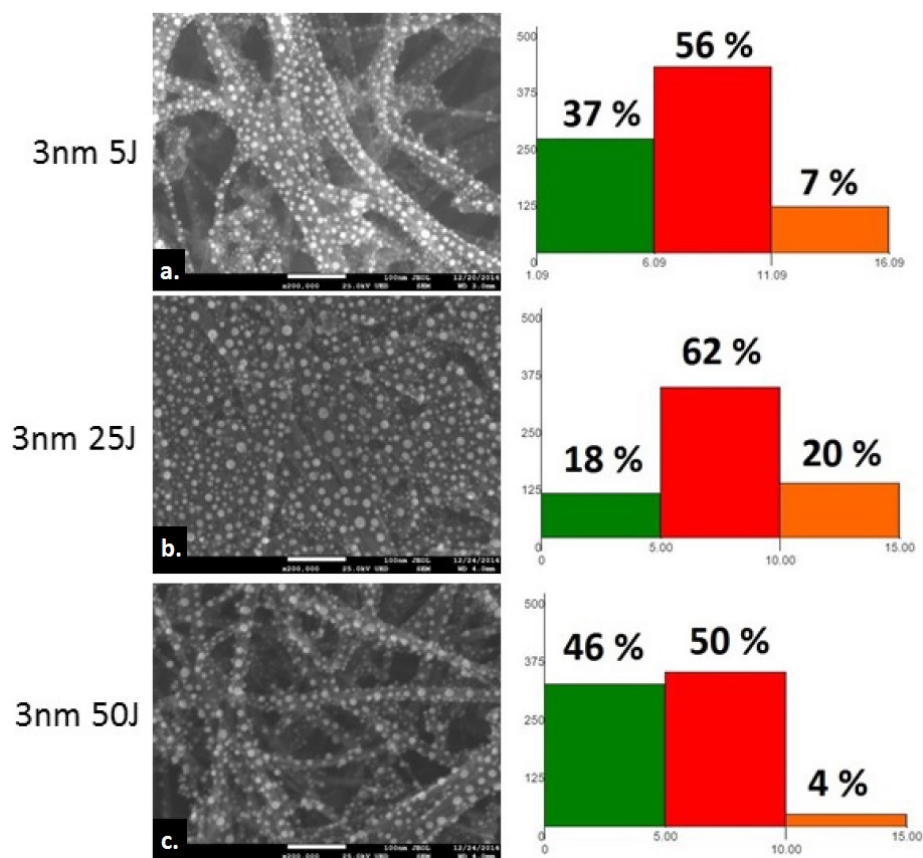
Figure 5.1. (a) SEM of the 3 nm initial thickness sample treated with 5 J/cm^2 single pulse of 2 ms duration. (b) SEM of the 3 nm initial thickness sample treated with 25 J/cm^2 single pulse of 2 ms duration (c) SEM of the 3 nm initial thickness sample treated with 5 J/cm^2.

that there are 37% of smaller sized particles and 56% of medium sized particles and only 7% of larger particles. With a 25 J/cm^2 pulse this scenario changes and complete nanoparticle formation occurs decreasing the population of smaller particles, this population is transferred to medium sized particles. Also the population of larger particles increases, which is the result of medium sized particles growing or undergoing coalition. With a 50 J/cm^2 of energy induction, the smaller sized particles increase which is the result of the process of evaporation of metal. The medium sized particles evaporate and transformed into smaller particles. Second significant change is that of larger particles which are almost eliminated, the evaporation decreases the population

of the larger particles to only 4%. It should be noted that there is also slight reduction in the population medium sized particles which is contributed by majority of the particles transforming into a smaller sized particles.

It is fair to comment that the processes of evaporation and coalition of particles starts concurrently, until there are no particles within the diffusion range. After such a condition is achieved the growth of particle size seizes and the reduction of size starts due to the evaporation process which continues to proceed.

5.2   6 nm and 9 nm

Similarly experiments done for 6 nm and 9 nm confirms the minimum dewetting energy of 20 J/cm^2 and 35 J/cm^2 respectively. Figure 5.2 shows the results of this experiment where energy was increased and for a 6 nm, 20 J/cm^2 of energy density was confirmed to be minimum required for dewetting. Figure 5.3 shows the results of the exactly similar experiment, and 35 J/cm^2 of energy density was confirmed for a 9 nm initial deposition. However the deposition of both 6 nm and 9 nm are both in the form of a continuous thin films.

Theoretically the range for 6 nm can be calculated to be 13.68 nm to 18.22 nm, which is parallel the experimentally obtained value of 12.81 nm. Similarly the theoretical value for 9 nm can be obtained to be from 24.78 nm to 35.14 nm, and the experimental value obtained is 22.69 nm. Also for both 6 nm and 9 nm initial thickness samples evaporation was observed at energy density of 50 J/cm^2.

5.3   15 nm and 30 nm

Similarly a higher initial thickness film of 15 nm to 30 nm was attempted, although a single shot of the maximum energy was not sufficient to dewet the thicker films, a multiple shots could dewet the film. 3 consecutive pulses of 50 J/cm^2 each with a gap duration of 2 ms could completely dewet a 15 nm film, where as a 30 nm film required 4 pulses. Figure 5.4 shows the results where the 15 nm sample, which is completely

Figure 5.2.   SEM images for visual comparison for 6 nm sample treated with single flash of (a) 5 J/cm^2, (b) 10 J/cm^2, (c) 15 J/cm^2, (d) 20 J/cm^2 energy density.

dewetted using 3 consecutive pulse. Similarly Figure 5.5 shows the results of a 30 nm film dewetted completely with 4 pulse.

However the size of particles were highly uneven for both 15 nm and 30 nm. Such an unevenness owes to the phenomenon of Ostwald ripening. Particles are said to be undergoing Ostwald ripening when smaller particles with a critical diffusion length fuse together to form a single particles with larger size. Such a process continues to occur until all particles with the diffusion rage are consumed. The unevenness of the distribution persists until there is no Ostwald ripening possible. There are primarily two factor contributing to this irregularity, the ripening of particles which adds to population of larger particles, a metal loss or evaporation process which primarily
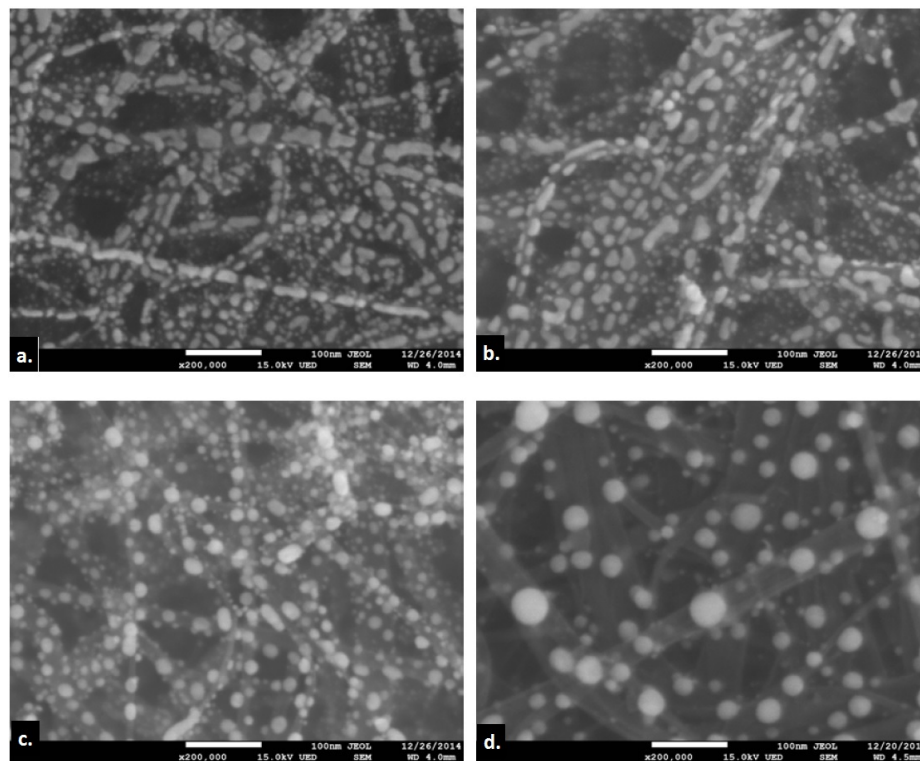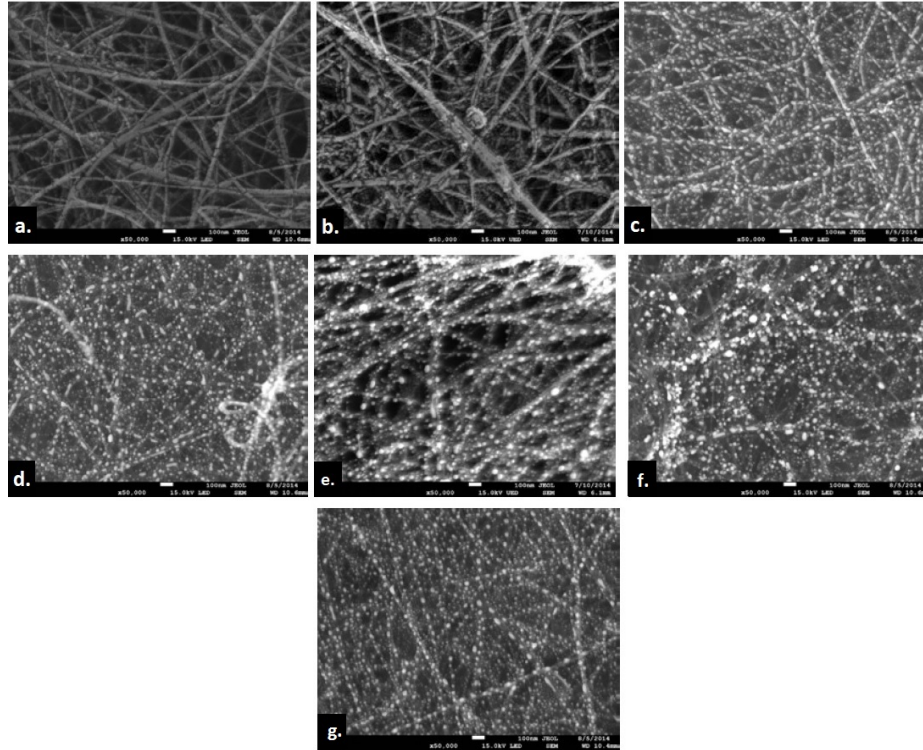
Figure 5.3. SEM images for visual comparison for 9 nm sample treated with single flash of (a) 5 J/cm^2, (b) 10 J/cm^2, (c) 15 J/cm^2, (d) 20 J/cm^2, (e) 25 J/cm^2, (f) 30 J/cm^2, (g) 35 J/cm^2 energy density.
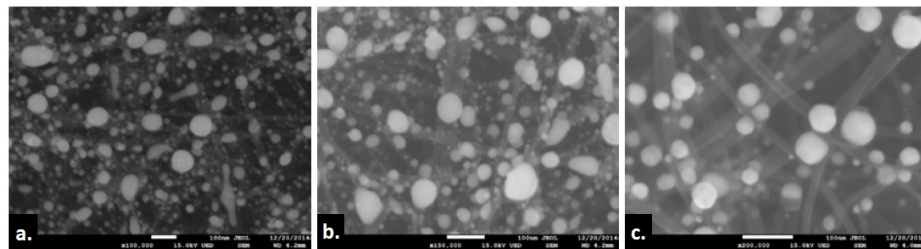
Figure 5.4. SEM images of 15 nm sample treated with (a) 1, (b) 2, (c) 3 consecutive pulses of 50 J/cm^2 of energy density.

adds to the reduction in size of medium size particles. The simultaneous growth and reduction induces unevenness.
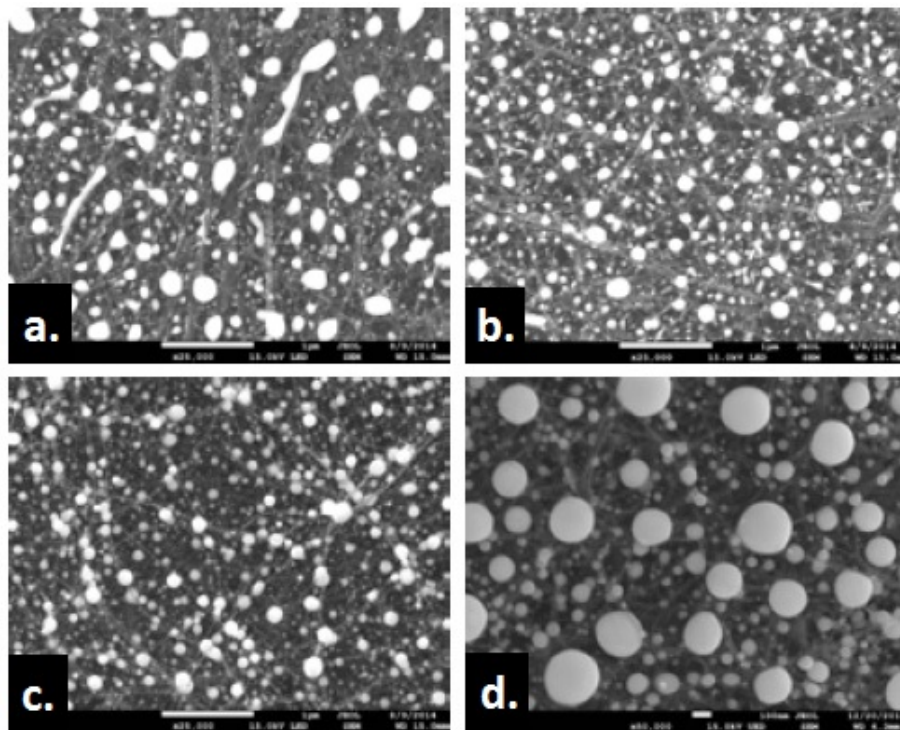
Figure 5.5. SEM images of 30 nm sample treated with (a) 1, (b) 2, (c) 3, (d) 4 consecutive pulses of 50 J/cm^2 of energy density.

5.4 Confirmation of Thermodynamic Stability

Experimental results revealed no significant change in size for both 6 nm and 9 nm samples. For a 6 nm sample, its minimum dewetting energy of 20 J/cm^2 was used. After transformation of film into complete spherical nanoparticles, dewetting was confirmed to be completed. After the completing and characterization and subsequent size analysis, the same sample was treated again with single flash of 20 J/cm^2. The sample was then characterized and the size of particles were analyzed. The single shot did not affect the size of the already dewetted nanoparticles owing to their thermodynamic stability. Further 5 more shots were fired and analysis was repeated. Figure 5.6 shows the visuals for comparison of the 6 nm sample.

Figure 5.6. SEM images of 5 stability checks of 6 nm sample treated with a single pulse of 20 J/cm^2 energy density.
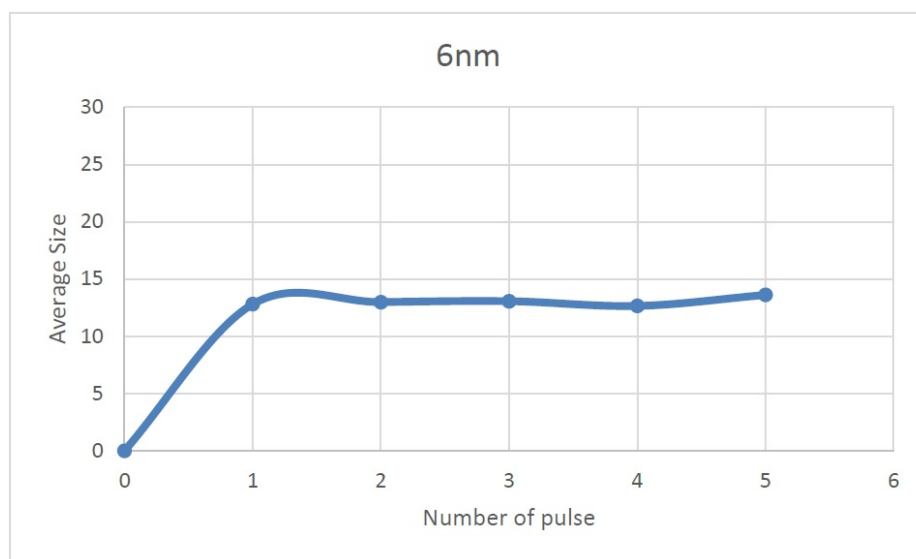
Figure 5.7. Graph of average diameter plotted against the pulse number of stability check for 6 nm initial film thickness.

The graph in Figure 5.7 represents the pulse number vs. the size of nanoparticles and it is clear that the size stabilizes a theoretical evidence of the observation is the standard deviation of the average sizes is 0.36 which is less than unity.

Similarly the 9 nm sample was treated, and 5 iteration were conducted. Figure 5.8 shows the visual confirmation and graph in Figure 5.9 confirms the hypothesis. From the graph shown in Figure 5.10 is another confirmation where the coefficient of variance for both 6 nm and 9 nm is less than 0.31 an 0.61 for 6 nm and 9 nm respectively.
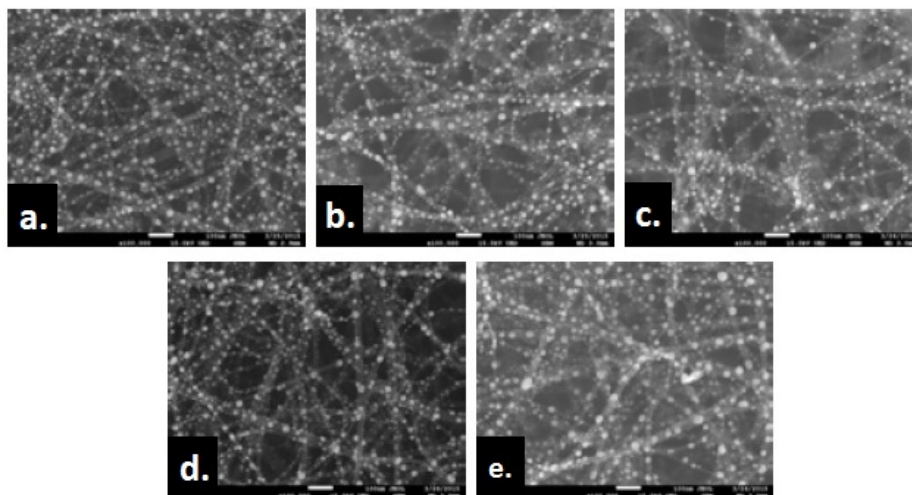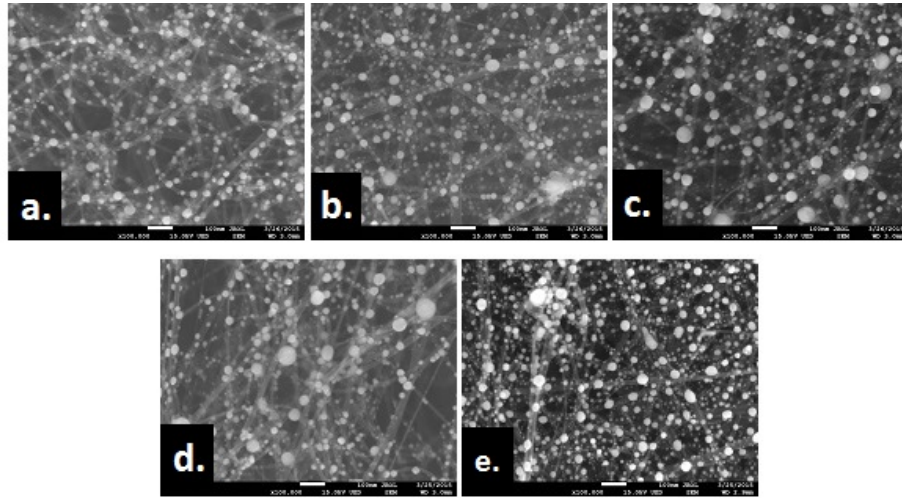

Figure 5.8. SEM images of 5 stability checks of 9 nm sample treated with a single pulse of 35 J/cm^2 energy density.

After this analysis it was concluded that the minimum dewetting energy is the magnitude of energy density, which can be used to produce nanoparticles in thermodynamic equilibrium.

5.5   Comparison with Conventional Thermal Annealing Process

The xenon flash induced dewetting is compared to the conventional thermal dewetting process. A 6 nm thin film was completely dewetted with a temperature of 300°C. A 4 h dewetting time was sufficient to completely dewet the film. Sample of 6 h and 10 h duration at the same condition confirmed that the size seized to grow and there was no ripening or evaporation of particles. This equilibrium stage was compared with flash annealed sample at the minimum dewetting energy. The conventional pro-
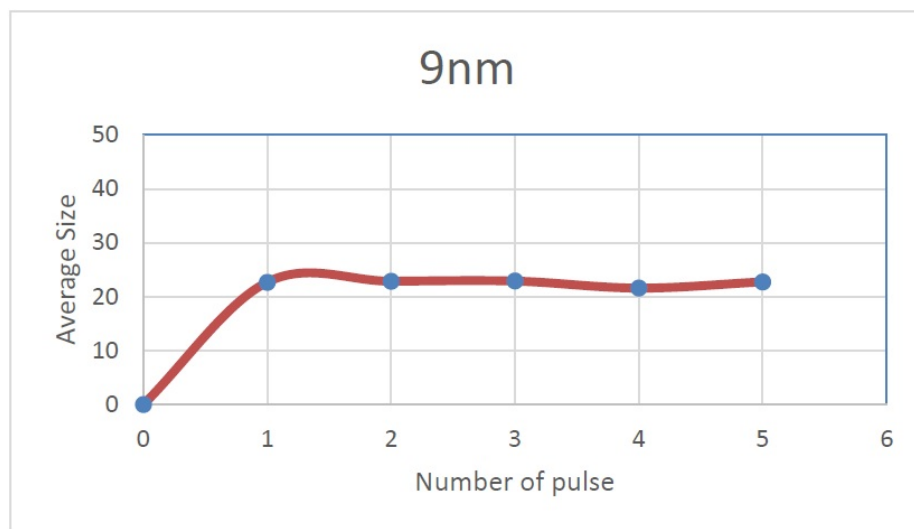
Figure 5.9.   Graph of average diameter plotted against the pulse number of stability check for 6 nm initial film thickness.
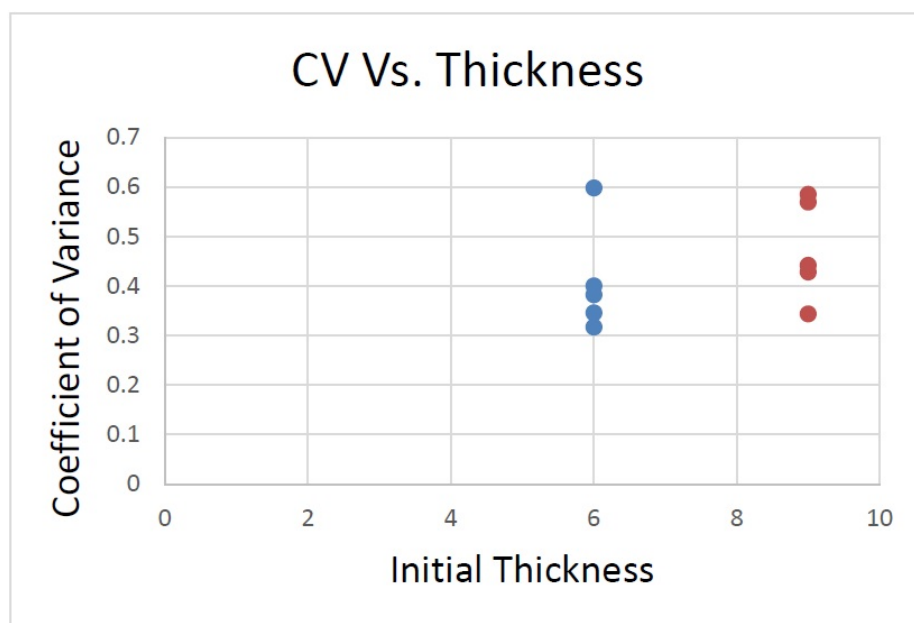
Figure 5.10. Graph of coefficient of variance plotted against the Initial thickness of film of stability check for 6 nm initial film thickness.

cess showed a size and standard deviation of 14.43 nm and 5.44 whereas, the flash annealed samples 12.82 nm and 4.06 respectively. Figure 5.11 visually compares the

Table 5.1.   List of Average diameters obtained from stability check, standard deviation and coefficient of variance.

Pulse	6 nm	9 nm
1	12.80628	22.69136
2	12.98885	22.88051
3	13.06444	22.90398
4	12.65028	21.60238
5	13.61161	22.75936
Avg. Diameter	13.02429	22.56752
Std. Dev.	0.365797	0.546534
Co. Eff. of Var.	0.028086	0.024218

SEM images of 6 nm sample thermally annealed at 300 °Cand Xenon flash annealed at 20 J/cm^2.
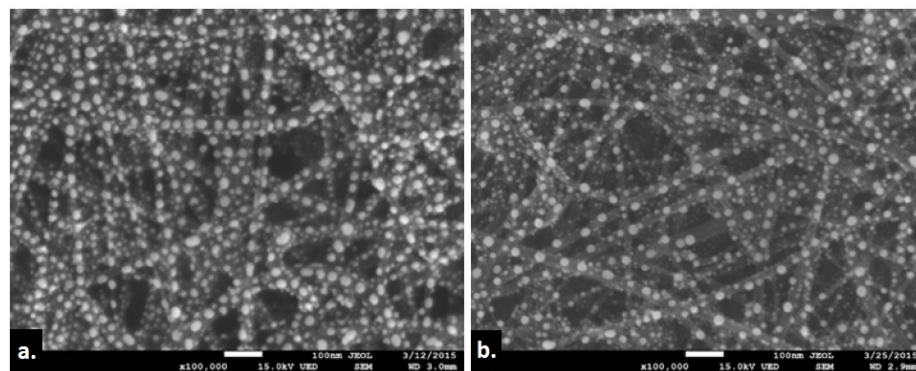
Figure 5.11.   (a) SEM image of 6 nm sample with completely thermodynamically stable nanoparticles formed by Thermal Annealing. (b) SEM image of 6 nm sample with completely thermodynamically stable nanoparticles formed by Xenon flash Annealing.

Table 5.2. Comparison of average size and standard deviation of 6 nm sample of the two Xenon flash annealing and conventional thermal annealing methods.

6 nm	Thermal Annealing	Xenon Flash Annealing
Average Size	13.02429461	14.88615966
Std. Dev.	6.657662	5.447451

Consistency of the process can be commented upon since the standard deviation of flash annealed sample is slightly lesser than conventional process. This difference in standard deviation suggests that the flash annealed dewetting is more consistent.
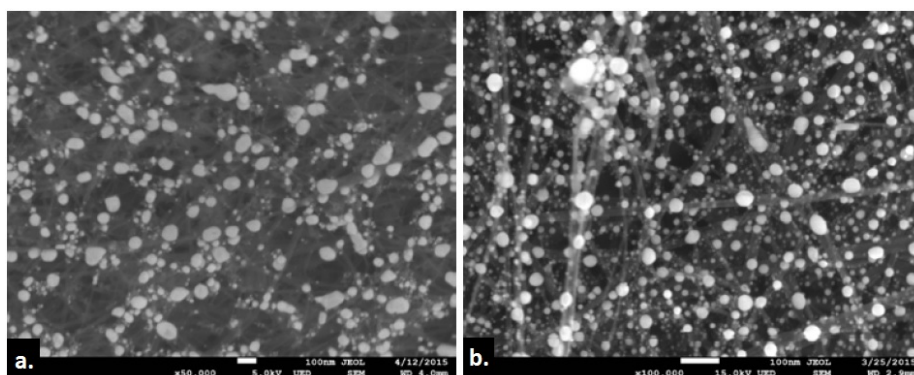
Figure 5.12. (a) SEM image of 9 nm sample with completely thermodynamically stable nanoparticles formed by Thermal Annealing (b) SEM image of 6 nm sample with completely thermodynamically stable nanoparticles formed by Xenon flash Annealing.

A similar trend is found in case of 9 nm, with a complete dewetting temperature of 400°C, size and standard deviation of thermal annealed sample was found to be 22.84 nm and 19.16 respectively. Whereas for the flash annealed sample the size was 22.56 nm and a standard deviation of 13.81 respectively. Figure 5.12 visually compares the SEM images of 9 nm sample thermally annealed at 400°Cand Xenon flash annealed at 35 J/cm^2.

Table 5.3.   Comparison of average size and standard deviation of 9 nm sample of the two xenon flash annealing and conventional thermal annealing methods

9 nm	Thermal Annealing	Xenon Flash Annealing
Average Size	22.84209	22.56751935
Std. Dev.	19.16605	0.546533664

6. CONCLUSIONS AND FUTURE WORK

From the SEM results it can be confirmed that the Xenon flash annealing can dewet a thin film into spherical nanoparticles.

The process of dewetting occurs forming elongated finger until a stage of completely spherical particles are formed. The coalition of particles continues until all smaller particles within the critical length are consumed, this process marks the process of complete dewetting. Further exposure to larger energy leads to evaporation which eliminates existing smaller particles but also create them simultaneously because to size reduction of larger particles.

It can also be concluded that the minimum dewetting energy and the evaporation energy are function of the initial film thickness.

From the experiments above it is clear that, it is possible to control the size of nanoparticle with a dry process and within a few seconds using xenon flash annealing process.

Obtaining particle size as a function of initial deposition energy input and number of pulse can be a good theoretical study which will be included in the future work. Also with an approach to scale the technology we have customized new xenon arc lamp which will be used to treat larger substrate to check the scalability of the process in future.

REFERENCES

REFERENCES

[1] C. Contado and A. Pagnoni, "Tio2 in commercial sunscreen lotion: flow field-flow fractionation and icp-aes together for size analysis," *Analytical chemistry*, vol. 80, no. 19, pp. 7594–7608, 2008.

[2] Z.-S. Wu, W. Ren, L. Wen, L. Gao, J. Zhao, Z. Chen, G. Zhou, F. Li, and H.-M. Cheng, "Graphene anchored with co3o4 nanoparticles as anode of lithium ion batteries with enhanced reversible capacity and cyclic performance," *ACS nano*, vol. 4, no. 6, pp. 3187–3194, 2010.

[3] L. Mai, L. Xu, C. Han, X. Xu, Y. Luo, S. Zhao, and Y. Zhao, "Electrospun ultra-long hierarchical vanadium oxide nanowires with high performance for lithium ion batteries," *Nano letters*, vol. 10, no. 11, pp. 4750–4755, 2010.

[4] D. H. Wang, D. Y. Kim, K. W. Choi, J. H. Seo, S. H. Im, J. H. Park, O. O. Park, and A. J. Heeger, "Enhancement of donor–acceptor polymer bulk heterojunction solar cell power conversion efficiencies by addition of au nanoparticles," *Angewandte Chemie*, vol. 123, no. 24, pp. 5633–5637, 2011.

[5] X. Zhou, Q. Wei, K. Sun, and L. Wang, "Formation of ultrafine uniform gold nanoparticles by sputtering and redeposition," *Applied physics letters*, vol. 94, no. 13, p. 133107, 2009.

[6] K. S. Soppimath, T. M. Aminabhavi, A. R. Kulkarni, and W. E. Rudzinski, "Biodegradable polymeric nanoparticles as drug delivery devices," *Journal of controlled release*, vol. 70, no. 1, pp. 1–20, 2001.

[7] I. Brigger, C. Dubernet, and P. Couvreur, "Nanoparticles in cancer therapy and diagnosis," *Advanced drug delivery reviews*, vol. 54, no. 5, pp. 631–651, 2002.

[8] X. Gao, Y. Cui, R. M. Levenson, L. W. Chung, and S. Nie, "In vivo cancer targeting and imaging with semiconductor quantum dots," *Nature biotechnology*, vol. 22, no. 8, pp. 969–976, 2004.

[9] M. C. Roco, "Nanoparticles and nanotechnology research," *Journal of Nanoparticle Research*, vol. 1, no. 1, pp. 1–6, 1999.

[10] Q. Jiang, M. Qu, G. Zhou, B. Zhang, and Z. Yu, "A study of activated carbon nanotubes as electrochemical super capacitors electrode materials," *Materials Letters*, vol. 57, no. 4, pp. 988–991, 2002.

[11] Y. Mu, H. Liang, J. Hu, L. Jiang, and L. Wan, "Controllable pt nanoparticle deposition on carbon nanotubes as an anode catalyst for direct methanol fuel cells," *The Journal of Physical Chemistry B*, vol. 109, no. 47, pp. 22212–22216, 2005.

[12] A. J. Haes and R. P. Van Duyne, "A nanoscale optical biosensor: sensitivity and selectivity of an approach based on the localized surface plasmon resonance spectroscopy of triangular silver nanoparticles," *Journal of the American Chemical Society*, vol. 124, no. 35, pp. 10 596–10 604, 2002.

[13] J. Li, Y. Zhao, N. Wang, and L. Guan, "A high performance carrier for sno 2 nanoparticles used in lithium ion battery," *Chemical Communications*, vol. 47, no. 18, pp. 5238–5240, 2011.

[14] E. Contés-de Jesús, J. Li, and C. R. Cabrera, "Latest advances in modified/functionalized carbon nanotube-based gas sensors," 2013.

[15] J. Han and C. Gao, "Functionalization of carbon nanotubes and other nanocarbons by azide chemistry," *Nano-Micro Letters*, vol. 2, no. 3, pp. 213–226, 2010.

[16] C. Favazza, R. Kalyanaraman, and R. Sureshkumar, "Robust nanopatterning by laser-induced dewetting of metal nanofilms," *Nanotechnology*, vol. 17, no. 16, p. 4229, 2006.

[17] A. B. Tesler, B. M. Maoz, Y. Feldman, A. Vaskevich, and I. Rubinstein, "Solid-state thermal dewetting of just-percolated gold films evaporated on glass: development of the morphology and optical properties," *The Journal of Physical Chemistry C*, vol. 117, no. 21, pp. 11 337–11 346, 2013.

[18] P. Farzinpour, A. Sundar, K. Gilroy, Z. Eskin, R. Hughes, and S. Neretina, "Altering the dewetting characteristics of ultrathin gold and silver films using a sacrificial antimony layer," *Nanotechnology*, vol. 23, no. 49, p. 495604, 2012.

[19] T. Zhang, M. B. Nix, B.-Y. Yoo, M. A. Deshusses, and N. V. Myung, "Electrochemically functionalized single-walled carbon nanotube gas sensor," *Electroanalysis*, vol. 18, no. 12, pp. 1153–1158, 2006.

[20] K. Balasubramanian and M. Burghard, "Chemically functionalized carbon nanotubes," *Small*, vol. 1, no. 2, pp. 180–192, 2005.

[21] M. S. Raghuveer, S. Agrawal, N. Bishop, and G. Ramanath, "Microwave-assisted single-step functionalization and in situ derivatization of carbon nanotubes with gold nanoparticles," *Chemistry of materials*, vol. 18, no. 6, pp. 1390–1393, 2006.

[22] L. Qu and L. Dai, "Substrate-enhanced electroless deposition of metal nanoparticles on carbon nanotubes," *Journal of the American Chemical Society*, vol. 127, no. 31, pp. 10 806–10 807, 2005.

[23] J. Lian, L. Wang, X. Sun, Q. Yu, and R. C. Ewing, "Patterning metallic nanostructures by ion-beam-induced dewetting and rayleigh instability," *Nano Letters*, vol. 6, no. 5, pp. 1047–1052, 2006.

[24] Y. Kojima and T. Kato, "Nanoparticle formation in au thin films by electron-beam-induced dewetting," *Nanotechnology*, vol. 19, no. 25, p. 255605, 2008.

[25] V. Datsyuk, M. Kalyva, K. Papagelis, J. Parthenios, D. Tasis, A. Siokou, I. Kallitsis, and C. Galiotis, "Chemical oxidation of multiwalled carbon nanotubes," *Carbon*, vol. 46, no. 6, pp. 833–840, 2008.

[26] W.-H. Pan, S. J. Lue, C.-M. Chang, and Y.-L. Liu, "Alkali doped polyvinyl alcohol/multi-walled carbon nano-tube electrolyte for direct methanol alkaline fuel cell," *Journal of Membrane Science*, vol. 376, no. 1, pp. 225–232, 2011.

[27] M. Prato, K. Kostarelos, and A. Bianco, "Functionalized carbon nanotubes in drug design and discovery," *Accounts of Chemical Research*, vol. 41, no. 1, pp. 60–68, 2007.

[28] M. Rahman, S. Zainuddin, M. Hosur, J. Malone, M. Salam, A. Kumar, and S. Jeelani, "Improvements in mechanical and thermo-mechanical properties of e-glass/epoxy composites using amino functionalized mwcnts," *Composite Structures*, vol. 94, no. 8, pp. 2397–2406, 2012.

[29] W. Wick, *A Drop Of Water: A Book of Science and Wonder.* Scholastic, 1997.

[30] J. D. Fowlkes, L. Kondic, J. Diez, Y. Wu, and P. D. Rack, "Self-assembly versus directed assembly of nanoparticles via pulsed laser induced dewetting of patterned metal films," *Nano Letters*, vol. 11, no. 6, pp. 2478–2485, 2011.

[31] G. Reiter, "Dewetting of thin polymer films," *Physical Review Letters*, vol. 68, no. 1, p. 75, 1992.

[32] L. Kondic, J. A. Diez, P. D. Rack, Y. Guan, and J. D. Fowlkes, "Nanoparticle assembly via the dewetting of patterned thin metal lines: Understanding the instability mechanisms," *Physical Review E*, vol. 79, no. 2, p. 026302, 2009.

[33] I. Beszeda, E. Gontier-Moya, and A. Imre, "Surface ostwald-ripening and evaporation of gold beaded films on sapphire," *Applied Physics A*, vol. 81, no. 4, pp. 673–677, 2005.

[34] D. Beke and Y. S. Kaganovskii, "Determination of parameters of surface mass transport from morphological changes of beaded thin films," *Materials Science and Engineering: B*, vol. 32, no. 3, pp. 185–199, 1995.

[35] A. Imre and D. Beke, "Determination of surface diffusion parameters of pd on sapphire from sem measurements of morphological changes of beaded films," *Applied Physics A*, vol. 72, no. 3, pp. 357–360, 2001.

[36] D. T. Danielson, D. K. Sparacin, J. Michel, and L. C. Kimerling, "Surface-energy-driven dewetting theory of silicon-on-insulator agglomeration," *Journal of Applied Physics*, vol. 100, no. 8, p. 083507, 2006.

[37] E. Jiran and C. Thompson, "Capillary instabilities in thin films," *Journal of Electronic Materials*, vol. 19, no. 11, pp. 1153–1160, 1990.

[38] D. J. Srolovitz and M. G. Goldiner, "The thermodynamics and kinetics of film agglomeration," *JOM*, vol. 47, no. 3, pp. 31–36, 1995.

[39] W.-S. Han, J.-M. Hong, H.-S. Kim, and Y.-W. Song, "Multi-pulsed white light sintering of printed cu nanoinks," *Nanotechnology*, vol. 22, no. 39, p. 395705, 2011.

[40] J. Ryu, H.-S. Kim, H. T. Hahn, and D. Lashmore, "Carbon nanotubes with platinum nano-islands as glucose biofuel cell electrodes," *Biosensors and Bioelectronics*, vol. 25, no. 7, pp. 1603–1608, 2010.

[41] J. Ryu, K. Kim, H.-S. Kim, H. T. Hahn, and D. Lashmore, "Intense pulsed light induced platinum–gold alloy formation on carbon nanotubes for non-enzymatic glucose detection," *Biosensors and Bioelectronics*, vol. 26, no. 2, pp. 602–607, 2010.

[42] J. Ryu, H.-S. Kim, and H. T. Hahn, "Reactive sintering of copper nanoparticles using intense pulsed light for printed electronics," *Journal of Electronic Materials*, vol. 40, no. 1, pp. 42–50, 2011.